Thermal liability of hyaloclastite in the Krafla geothermal reservoir, Iceland: the impact of phyllosilicates on permeability and rock strength

Josh Weaver[1], Guðjón H. Eggertsson[1], James E.P. Utley[1], Paul A. Wallace[1], Anthony Lamur[1], Jackie E. Kendrick[1], Hugh Tuffen[2], Sigurður H. Markússon[3], Yan Lavallée[1].

[1]Department of Earth, Ocean and Ecological Sciences, University of Liverpool, 4 Brownlow Street, L69 3GP, Liverpool, UK

[2]Lancaster Environment Centre, Lancaster University, LA1 4YQ, Lancaster, UK

[3]Landsvirkjun, Háaleitisbraut 68, 110 Reykjavík, Iceland

j.weaver@liverpool.ac.uk

Keywords: Krafla, basaltic hyaloclastite, thermal stress, smectite, mechanical properties, geothermal, clay mineralogy

Abstract

Geothermal fields are prone to temperature fluctuations from natural hydrothermal activity, anthropogenic drilling practices, and magmatic intrusions. These fluctuations may elicit a response from the rocks in terms of their permeability, mineralogical and mechanical properties. Hyaloclastites are a highly variable volcaniclastic rock predominantly formed of glass clasts that are produced during non-explosive quench-induced fragmentation, in both subaqueous and sub-glacial eruptive environments. They are common in high-latitude geothermal fields as both weak, highly permeable reservoir rocks and compacted impermeable cap rocks. Basaltic glass is altered through interactions with external water into a clay-dominated matrix, termed palagonite, that acts to cement the bulk rock. The abundant, hydrous phyllosilicate minerals within the palagonite can dehydrate at elevated temperatures, potentially resulting in thermal liability of the bulk rock.

Using surficial samples collected from Krafla, northeast Iceland, and a range of petrographic, mineralogical and mechanical analyses, we find that smectite dehydration occurs at temperatures commonly experienced within geothermal fields. Dehydration events at 130, 185 and 600 °C result in progressive mass loss and contraction. This evolution results in a positive correlation between treatment temperature, porosity gain and permeability increase. Gas permeability measured at 1 MPa confining pressure shows a 3-fold increase following thermal treatment at 600 °C. Furthermore, strength measurements show that brittle failure is dependent on porosity and therefore the degree of thermal treatment. Following thermal treatment at 600 °C, the indirect tensile strength, uniaxial compressive strength and triaxial compressive strength (at 5 MPa confining pressure) decrease by up

to 68% (1.1 MPa), 63% (7.3 MPa) and 25% (7.9 MPa), respectively. These results are compared with hyaloclastite taken from several depths within the Krafla reservoir, through which the palagonite transitions from smectite- to chlorite-dominated.

We discuss how temperature-induced changes to the geomechanical properties of hyaloclastite may impact fluid flow in hydrothermal reservoirs and consider the potential implications for hyaloclastite-hosted intrusions. Ultimately, we show that phyllosilicate-bearing rocks are susceptible to temperature fluctuations in geothermal fields.

1. Introduction

Reservoir rocks in geothermal fields are exposed to thermal fluctuations from natural (Ármannsson et al., 2013) as well as anthropogenic temperature sources (De Simone et al., 2013). These fluctuations range from ~250 °C of cooling during thermal stimulation practices (Tulinius et al., 2000) to heating of up to 400 °C during flow testing (Axelsson, 2012) and up to ~1200 °C during basaltic magma intrusions (Schauroth et al., 2016). Importantly for the sustainability of hydrothermal systems, temperature variations cause volumetric changes that may impart damage (Browning et al., 2016; Coats et al., 2018; Eggertsson et al., 2018; Heap et al., 2013b; Kendrick et al., 2013; Schaefer et al., 2015; Siratovich et al., 2014) and have the potential to trigger mineral reactions, prompting precipitation or breakdown (*e.g.* Ghassemi and Kumar, 2007) in altered reservoir rocks (Bird et al., 1984). These reactions can affect key reservoir rock properties, such as porosity, permeability and strength (*e.g.* Heap et al., 2013a), that may influence the capacity for fluid circulation (Kumar and Ghassemi, 2005; Siratovich et al., 2015) and thus dictate energy production potential (Clearwater et al., 2015). Understanding the lithology-specific development of these properties in response to temperature is important for improved fluid flow modelling in geothermal fields.

Hyaloclastite is a rock type prevalent in subaqueous and high-latitude, glaciated regions such as Iceland, where it forms a major reservoir constituent in several geothermal fields (Kristmannsdóttir, 1979; Marks et al., 2010; Mortensen et al., 2014). It is often highly porous and permeable, such that it is frequently targeted for geothermal production, shallow freshwater aquifers or carbon reinjection and mineralisation (Kim et al., 2009; Matter et al., 2011; Zakharova and Spichak, 2012) but it is also weak and can collapse to form a mechanically sealed, impermeable caprock (Nielson and Stiger, 1996). Hyaloclastites are highly variable, altered volcaniclastic breccias that form explicitly by severe quench-induced fragmentation of magma interacting with a large volume of external water or ice (Wohletz, 1986). However, the term is often applied ambiguously in literature to any lava fragmented by interaction with water (Honnorez and Kirst, 1975); consequently, it is commonly identified in a wide range of water-rich environments, such as mid-ocean ridges (Hekinian et al., 2000), seamounts (Davis

and Clague, 2003; Mitchell, 2003), sub-marine volcanic flanks (Ferrer et al., 2010; Schiffman et al., 2006), subglacial tuyas (Jakobsson and Gudmundsson, 2008), tindar ridges (Jarosch et al., 2008; Schopka et al., 2006), nearshore waters (Bergh and Sigvaldason, 1991) and emergent islands (Kokelaar, 1986; Wohletz and Sheridan, 1983). Therefore, hyaloclastite is more appropriately considered a non-genetic term (Wright and Cas, 1988) that is more accurately defined by the descriptive lithological criteria, used herein, of quench fragmented sideromelane (*i.e.*, basaltic glass) supported by a palagonite matrix (Van Otterloo et al., 2015). This is in contrast to the largely cohesionless perlite, that is produced following the hydration-induced alteration of dacitic and rhyolitic glass (Denton et al., 2009).

The abundance of palagonite in hyaloclastites arises from the inherent metastable nature of basaltic volcanic glass exposed to fluids (Oelkers and Gislason, 2001), especially at moderate to high temperatures (Cerling et al., 1985; von Aulock et al., 2013). Palagonite is considered the first alteration product of mafic glass; it forms initially as an amorphous phase during the complex, concurrent processes of glass hydration and devitrification (Berger et al., 1987; Stroncik and Schmincke, 2001). The crystallographic character of palagonite is time-dependent, transitioning from a clear amorphous phase displayed in concentric bands of gel-palagonite, to a highly variable assortment of crystal habits (*e.g.*, fibrous, lath-like or granular structure) termed fibro-palagonite. Fibro-palagonite is commonly dominated by clays, namely smectite, and zeolites (Drief and Schiffman, 2004; Franzson et al., 2010).

Rocks comprised of clay and zeolite minerals tend to be highly sensitive to moderate thermal fluctuations on the order of a few hundred degrees Celsius (*e.g.*, Heap et al., 2012). In particular, high temperatures may trigger devolatilisation reactions that prompt the breakdown of these minerals. This occurrence leads to a loss of material that results in the creation of porosity, thereby affecting the strength and permeability of the rock (Bedford et al., 2018; Bernabé et al., 2003; Heap et al., 2012). This is also true for incomplete reactions in rocks experiencing short excursions to high temperature (Mordensky et al., 2019). In the case of palagonite undergoing a temperature increase, dehydration can begin below 200 °C and result in greater mass loss than in many other clays (Milliken and Mustard, 2005). This suggests hyaloclastite may be particularly susceptible to thermally induced devolatilisation reactions that are likely to affect geomechanical properties (Heap et al., 2012).

Here, we investigate the impact of thermal treatment on hyaloclastite, constraining the mineralogical, mechanical and physical evolution at a range of temperatures up to 600 °C.

2. Material and Methods

2.1 Overview

Samples were initially characterised using a suite of thermal analysis equipment in order to select a series of treatment temperatures at which the hyaloclastite would be analysed in further detail. After fully characterising the mineralogical, physical and mechanical properties of the as-collected material, cores were dwelled at the selected treatment temperature and cooled to room temperature, petrographic observations were made and the impact on mineralogy, mass, porosity, permeability and strength was determined.

2.2 Materials

Krafla caldera, located in north-east Iceland (Fig. 1), hosts a well-developed geothermal field operated by Landsvirkjun, the national power company of Iceland. The caldera infill is dominated by hyaloclastite and basaltic intrusions to a depth of 1300 m (Mortensen et al., 2014), which comprise the reservoir rock hosting hydrothermal fluids harnessed for heating and energy production (Gudmundsson and Arnórsson, 2002). The surficial sample block was collected from the south eastern caldera edge (65°N 41.067; -16°W 43.089) in August 2015, where the outcrops protrude from the surface and are isolated from the hydrothermal reservoir, thus undergoing trivial debilitation from exposure to the high-temperature reservoir fluids. However, the youngest and shallowest hyaloclastites at Krafla formed during the last glacial period (Ármannsson et al., 1987) and have possibly been buried and then subsequently exhumed due to glacial erosion (Tuffen and Castro, 2009). To complement these 'fresh' samples, a limited suite of subsurface samples were retrieved during the coring of boreholes KH-4 (70 m) and KH-6 (556 m and 732 m) by Landsvirkjun. The in-situ sample temperatures were recorded during and after drilling of the wells; the 70-m sample from KH-4 was measured at 41 ˚C during drilling, while after leaving borehole KH-6 to thermally equilibrate for one week, the 556-m and 732-m depths were measured at 145 and 125 ˚C, respectively (Gautason et al., 2007). Note that the sample collected from 556 m depth may have interacted with a basaltic dyke, located approximately 1 m below. The surficial sample was chosen to ensure it was texturally representative of the local geology and similar to the subsurface samples in terms of clast size and abundance. Upon visual inspection, the selected sample was relatively homogenous and lacked large features such as fractures or clasts greater than 1 cm in diameter. For all mechanical and permeability measurements, heterogeneities were limited to less than 10 % of the sample size of 26 mm by 52 mm for cores and 26 mm by 13 mm for discs. Following sample preparation and prior to all testing, samples were oven dried at 70 °C for 4 hours and subsequently stored in a desiccator at room temperature. All samples were prepared, characterised and tested at the University of Liverpool.

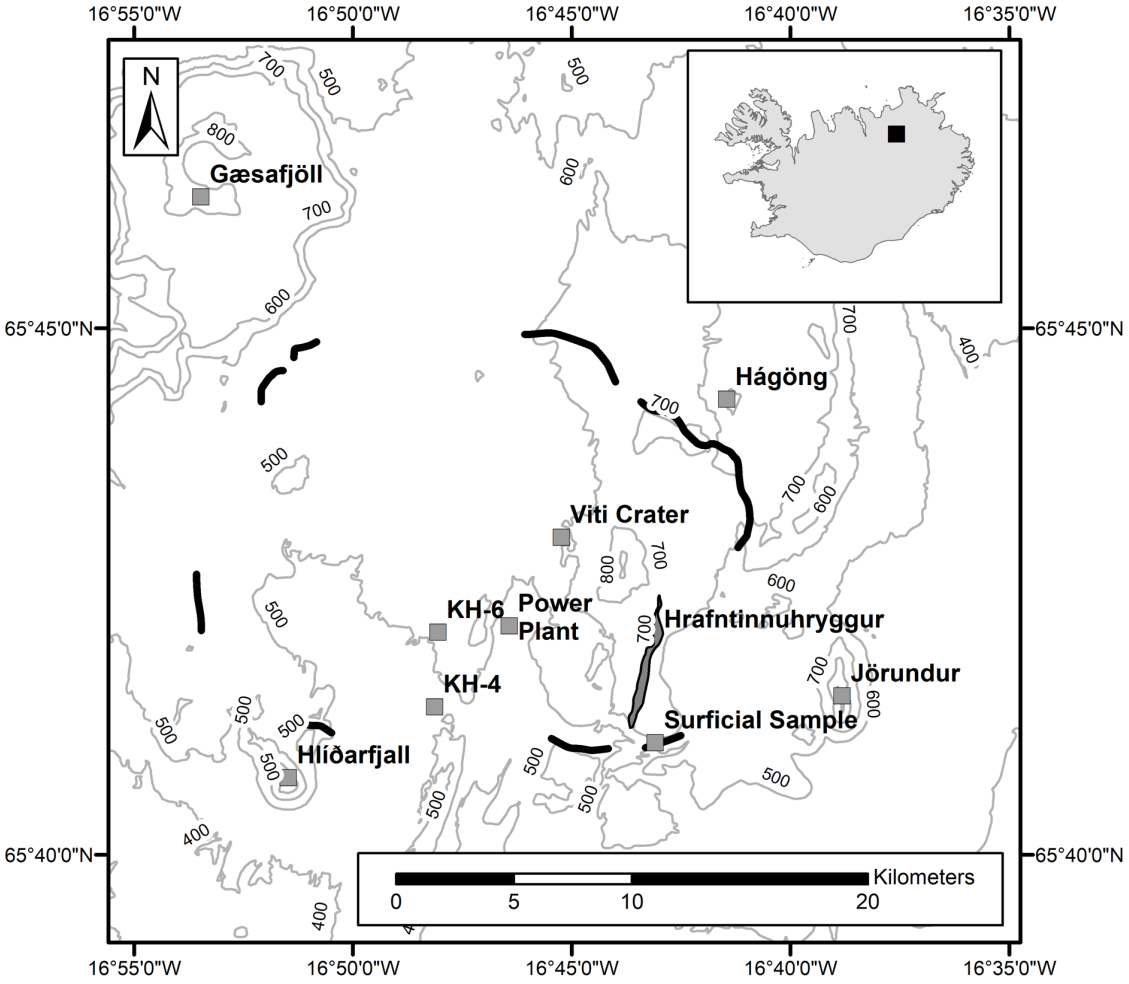

Figure 1. A map of the Krafla geothermal field showing the location of the surficial sampling site, subsurface sampling sites (boreholes KH-4 and KH-6), the Krafla power plant and local geomorphological features. Faults associated with the Krafla caldera complex are marked in black.

2.3 Simultaneous Thermal Analysis (STA)

Mass loss and heat capacity were measured against temperature concurrently in a Netzsch STA 449 F1 Jupiter using simultaneous thermal analyser (STA), which combines thermo-gravimetric analysis and differential scanning calorimetry (TGA-DSC). Samples were cored to 6 mm by 1 mm discs and loaded into a platinum crucible. Prior to each test run, the sample chamber was purged with argon gas and exhausted to vacuum conditions. Each test was initially conducted with an empty crucible to provide a correction baseline, a second time containing a sapphire standard with the same sample dimensions, to correlate the DSC data, and a final time containing the hyaloclastite sample. All temperature profiles were initially heated to 50 °C at 2 °C/min for a 10 minute isothermal period. For surficial samples, constant-rate temperature profiles, heated to 700 °C at 5 °C, 10 °C and 20 °C/min, as well as stepped isothermal profiles, consecutively heated to each treatment temperature at 5

°C/min consecutively and dwelled for 12 hours, were conducted. For subsurface samples, constant-rate temperature profiles were heated to 700 °C at a rate of 10 °C/min only. Data was collected from 50 °C at a 0.1 minute resolution, with mass accurate to 0.025 µg and heat capacity to ±2%.

2.4 Thermo-Mechanical Analysis (TMA)

Absolute thermal expansion coefficients were recorded using a Netzsch TMA 402 F1 Hyperion. Samples were cored to 6 mm diameter by 5 mm height cylinders. A core sample was loaded between the piston of the TMA and the furnace was sealed shut around the sample assembly. Prior to each test, the sample chamber was purged with argon gas and exhausted to vacuum conditions. For each test the temperature and load profile were completed twice; initially a ceramic cylinder, matching the sample proportions to within 5%, was used to supply a correction base-line that was removed from the second test run containing the hyaloclastite sample; this allowed an accurate determination of the sample length changes. All temperature profiles were initially heated to 40 °C at 2 °C/min for a 10 minute isothermal period. Constant rate temperature profiles, heated to 700 °C at 5 °C, 10 °C and 20 °C/min were completed using a 1 N load. Data was collected at a 0.01 minute resolution, with height change accurate to 1.25 nm and load to 0.01 mN.

2.5 Thermal Treatment

Thermal treatment temperatures of 130 °C, 185 °C, 400 °C and 600 °C were selected following TGA-DSC and TMA measurements. Sample cores, 26 mm by 52 mm, and Brazilian discs, 26 mm by 13 mm, were thermally treated in a Carbolite CWF1300 box furnace, to be compared against as-collected samples. Samples were heated at 5 °C/min and, once at target temperature, were left to dwell for 12 hours before being cooled to room temperature at a rate of 5 °C/min.

2.6 Mineralogical Analysis

Mineralogical and textural changes at each treatment temperature were investigated using a combination of X-Ray Diffraction analysis (XRD), optical microscopy and quantitative evaluation of minerals by scanning electron microscopy (QEMSCAN). Adjacent samples were cored and subjected to the temperature profile for each of the treatment temperatures discussed above in order to prepare samples for mineralogical analysis; part of these rocks were cut for thin section preparation and the rest was crushed to powder (see below). Adjacent samples were selected to minimise potential mineralogical differences from within the hyaloclastite, which are petrogenetically heterogeneous.

XRD analysis was completed on dried, glycolated and clay-separated samples using a Panalytical X'Pert Pro MPD diffractometer fitted with an X'Celerator detector. Texturally representative rocks were crushed, in distilled water, to a powder <10 µm using an agate McCrone micronizing mill and

subsequently dried at 60°C before being further crushed into a loose powder using an agate pestle and mortar. Clay separated samples were partially crushed in a ceramic pestle and mortar, and then prepared with ultrasonication in distilled water, with the equivalent spherical particle size selected for by standard centrifugation methods. Clay separated samples were then dried at 60 °C and re-crushed into a light random powder. For glycolated samples, saturation of a random powder was achieved by using ethylene glycol by vapour pressure at 60 °C, for 24 hours. Samples were back loaded into cavity holders as random powders. A Copper X-ray tube was used, with Ni filter to select for Cu k-α radiation. Scans covered the 2Theta range of 4-70°2θ. Data was analysed using the Relative Intensity Ratio (RIR) method within the HighScore Plus® software, alongside reference patterns from the International Centre for Diffraction Data, Powder Diffraction File-2 Release 2008.

Mineral distribution was imaged at 20 µm resolution for each thin section, and at 4 µm resolution for selected sites, using Scanning Electron Microscope Energy Dispersive X-Ray Spectroscopy (SEM-EDS) on uncovered, carbon-coated thin sections imbedded with luminescent dye. Using a QEMSCAN developed by FEI, elemental chemistry was mapped and quantified using two Bruker EDS detectors and matched to known compositions of minerals and glasses. Crystallographic features are not recorded, preventing the differentiation of polymorphs and mineral dissociation (in the case where chemical transport is limited). Mineral and glass abundance was quantified at 20 µm resolution by comparing the relative proportions of pixels in each image, normalised against the pore space.

2.7 Porosity Determination

Prior to and following thermal treatment, the skeletal volume of each sample (*i.e.*, the volume of solid rock, including isolated pore space) was measured using a Micromeritics AccuPyc II 1340 Helium Pycnometer, accurate to ±0.1% of the measured volume. The connected porosity (ϕ), into which fluids are able to flow, was then determined by the ratio of measured skeletal volume (V_m) to the volume calculated by the core dimensions (V_c), such that:

$$\phi = \frac{V_c - V_m}{V_c} \qquad \text{Eq. 1}$$

2.8 Permeability Measurements

Gas permeability was measured for each sample core, prior to and following thermal treatment, using a Vinci Technologies gas permeameter with nitrogen gas. The 26 mm by 52 mm sample cores were inserted into a compressible Viton jacket and loaded to 1 MPa confining pressure using a manual valve. Gas flow was automatically set to a constant rate through the sample, which increased by a factor of 2 until a differential pressure of >0.5 psi was achieved between the inlet and outlet. The flow rate values ranged from 33 to 190 cm^3/min. The sample permeability (*k*) was calculated using Darcy's law:

208 $$Q = \frac{-kA\,\Delta P}{\mu L}$$ Eq. 2

209 where Q is the flow rate, A is the cross-sectional surface area of the sample, ΔP is the pressure
210 differential, accurate to 1% full scale, measured across the sample, μ is the viscosity of the liquid (in
211 this case nitrogen), and L is the sample length.

212 For selected cores, steady-state water permeability was also measured in a hydrostatic loading cell
213 from Sanchez Technologies. Within the load cell, the 26 mm by 52 mm sample cores were inserted
214 into an impermeable Viton jacket and loaded to the desired effective pressure (confining pressure –
215 pore pressure). Confining pressure was applied using low-viscosity silicone oil and pore pressure was
216 applied using de-mineralised water. Permeability was measured by maintaining 2 MPa of pore
217 pressure at one side of the sample and 1 MPa of pore pressure at the other, such that a constant 1
218 MPa pressure differential was upheld with an average pore pressure of 1.5 MPa, and the flow rate
219 was measured, accurate to 0.01 ml/min. For each sample, the permeability was measured at 5 MPa
220 confining pressure increments consecutively, up to 30 MPa, to simulate depths up to and in excess of
221 the deepest hyaloclastite units at Krafla. To ensure permeability was measured under steady-state
222 conditions and that no gas slippage was occurring, the need for Klinkenburg (Klinkenberg et al, 1941)
223 and Forcheimer (Forchheimer, 1901) corrections was assessed for each sample and found to not be
224 required for any of the samples in both the gas and water permeameters.

225 Porosity change associated with fracture closure during loading was also recorded in the hydrostatic
226 cell, prior to each permeability measurement (after Eggertsson et al., 2018), using the monitored
227 volume of water that was expelled from the sample. However, absolute porosity variations are not
228 reported as volume change is not monitored during the first loading step, instead the porosity
229 reduction (%) is calculated from the initial porosity measured by Helium pycnometry. Note that due
230 to potential damage inflicted during loading, samples measured in the hydrostatic load cell were not
231 used for subsequent strength testing.

232 ## 2.9 Strength Measurements

233 Uniaxial and triaxial compressive strength tests and indirect tensile strength tests were performed on
234 as-collected as well as thermally treated (TT) samples at dry, ambient room temperature conditions.

235 The uniaxial compressive strength (UCS) of the rocks was determined using an 8800 Instron uniaxial
236 press. Cylindrical rock cores, for which porosity and gas permeability had been measured, were loaded
237 at a constant strain rate of 10^{-5} s^{-1} until failure. Load was recorded with a resolution of 0.1 s at 10 Hz.

238 The compressive triaxial strength (TXL) of cores subjected to various confining pressures was
239 measured using a Sanchez Technologies TRIAX100 press. Here again, cylindrical rock cores for which

porosity and permeability had been determined were placed between the pistons and jacketed using an impermeable Viton sleeve. The sample assembly was subjected to confining pressure (P_c) by introducing argon gas in the pressure vessel; 5 MPa confining pressure was applied to each sample whilst a constant 1 MPa differential stress was maintained by controlling the axial load. Note that no pore pressure was applied, so that the confining pressure is equivalent to the effective pressure. Upon reaching the confining pressure, the sample was axially deformed at a strain rate of 10^{-5} s^{-1} until rupture, denoted by a stress drop in the mechanical data, or until a stress plateau was reached. The confining pressure, pore pressure, axial stress and sample deformation were recorded at 1 s resolution.

Young's modulus, calculated by dividing stress over strain, was derived using the gradient of the manually defined, elastic linear loading section of each uniaxial and triaxial strength curve.

The indirect tensile strength (UTS) of the samples was measured by employing the Brazilian disc method using a 5969 Instron uniaxial press. Here, cylindrical discs, 26 mm diameter by 13 mm thickness, were radially loaded at a constant deformation rate of 26 µm/s until a stress drop was recorded, associated with failure. Sample deformation, accurate to ±0.1 µm, and load were recorded with a resolution of 0.05 s, and the tensile strength, σ_t, was calculated following the ASTM 2008 standard:

$$\sigma_t = \frac{2P}{\pi LD} \qquad \text{Eq. 3}$$

where P is the maximum applied load (N) and L and D are the thickness and diameter of the specimen (mm), respectively.

Note that the mechanical data was corrected for compliance of the loading frame of each press in accordance with the ASTM D7070-16 standard procedure.

3. Results

3.1 Simultaneous Thermal Analysis

Thermo-gravimetric analysis (TGA) reveals progressive, nonlinear mass loss upon heating above 50 °C (Fig. 2a). For the surficial samples (referred to as 0m), mass loss is initially negatively correlated with heating rate, whereby mass is lost more rapidly at low heating rates; however, beyond 250 °C there is no correlation and the mass loss at 700 ˚C ranges from 7 to 10 %, reflecting sample heterogeneity. In contrast, the subsurface samples (referred to by their sampling depths of 70 m, 556 m, and 732 m) have distinct multistep mass loss shoulders around 100-200 °C and 475-600 °C; yet, the magnitude of

mass loss in each of these temperature ranges varies with depth. Ultimately the fraction of mass lost is higher in surficial samples than in subsurface samples.

Differential scanning calorimetry measurements associated with the above thermo-gravimetric analysis reveal further details associated with the mass loss events (Fig. 2b). The surface samples show double-shouldered endothermic peaks at 130 °C and 185 °C (Fig. 2b), consistent with the 100-200 °C mass loss event recorded by the TGA (Fig. 2a). With increased heating rate, the endothermic peaks are pushed to slightly higher temperatures (up to ~ 150 °C and 220 °C at 20 °C/min). At a higher temperature, a faint shoulder develops around 300 °C and a broad, low-magnitude peak is evident around 650 °C; yet neither correspond to distinct mass loss events in Figure 2a. In contrast, the subsurface samples exhibit a less substantial double-shouldered peak at 130 °C and 185 °C than the surficial samples and faint, broad peaks around 300 °C; however they display strong endothermic peaks at high temperatures: for the 70-m sample a wide peak develops between 550 °C and 660 °C; for the sample from 556 m the data shows a peak at 525 °C, and for the sample from 732 m, the data show a peak at 560 °C.

Based on the simultaneous thermal analysis (Fig. 2a, b) four temperatures were selected as thermal treatment targets: 130, 185, 400 and 600 °C. Results from 12 hour-isothermal TGA measurements at these temperatures show that mass reaches a new stable value over long time periods, resulting in mass loss of 5%, 5.8%, 7.1% and 7.5%, respectively (Fig. 2c).

3.2 Thermo-Mechanical Analysis (TMA)

Thermo-mechanical analysis was employed to constrain the length changes associated with the mass loss events observed in Figure 2a. Surface samples initially exhibit limited thermal expansion, followed by minor contraction between 110 °C and 290 °C (Fig. 2d). A return to limited thermal expansion ends at 500 °C, after which significant contraction occurs. The temperature of the maximum extent of contraction between 110 °C and 290 °C and the rate of collapse beyond 500 °C are positively correlated with heating rate. Subsurface samples from 70 m depth show moderate expansion up to 475 °C, at which point expansion ceases, before rapidly accelerating beyond 640 °C. Note that a visual inspection of the two 70-m samples, following the TMA analysis, indicated the occurrence of vesiculation of the glass phase; we do not study this further as no surficial samples underwent such a process. The 556-m sample is entirely dominated by thermal expansion up to 700 °C, whilst the 732-m expands rapidly up to 185 °C and collapses beyond ~575 °C.

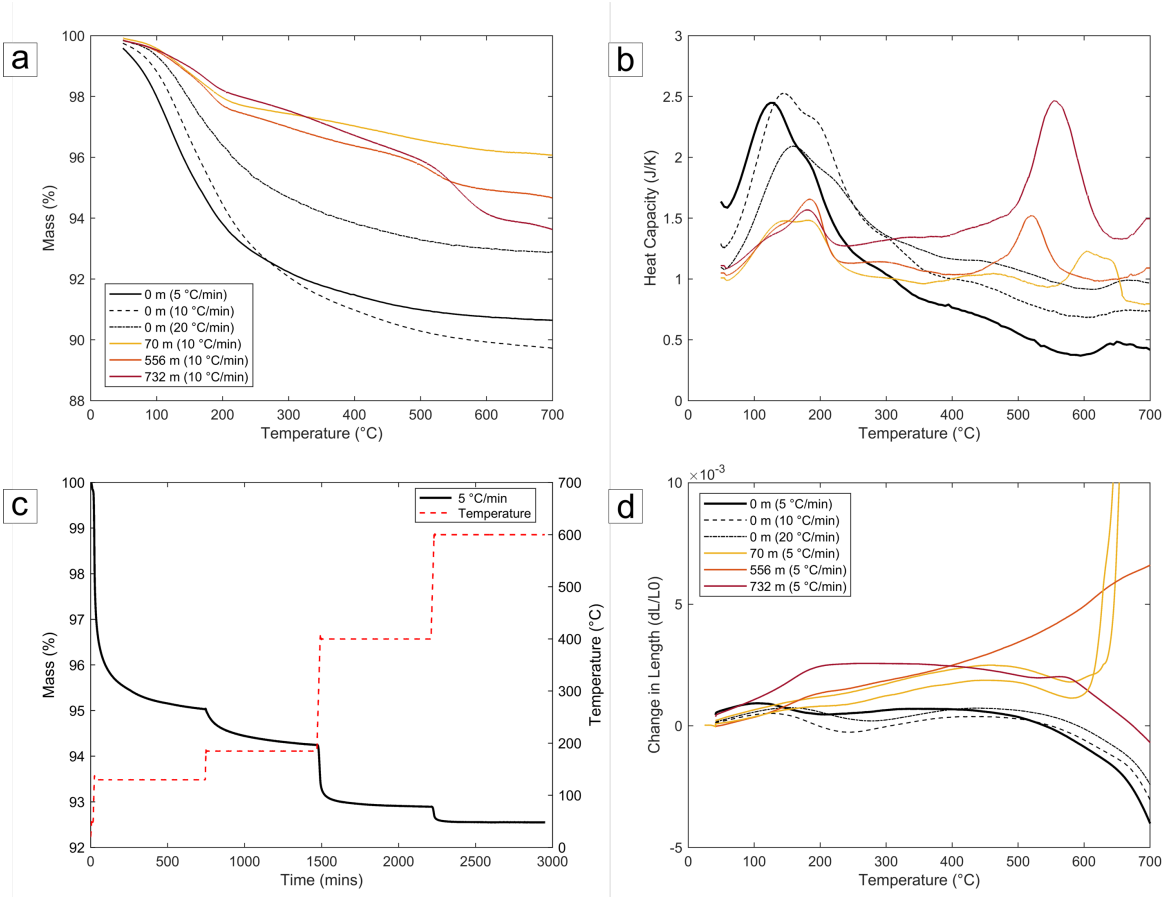

Figure 2 – Thermal analysis using TGA-DSC and TMA. a. Fixed-rate TGA showing thermal-induced mass loss for surficial and subsurface hyaloclastite; b. Fixed-rate DSC showing low-temperature heat capacity peaks against temperature for surficial samples and high-temperature peaks for subsurface samples; c. TGA showing mass loss during sequential 12-hour isothermal dwells, for surficial hyaloclastite; d. Fixed-rate TMA for surficial and subsurface samples, showing volumetric collapse for surficial material and a range of depth-dependent responses for subsurface material.

3.3 Mineralogical Analysis

A range of mineralogical and petrographic techniques were applied to further investigate the crystallographic and textural impact of suspected reactions. XRD analysis (Table 1) shows that the surficial hyaloclastite is primarily comprised of the common mafic igneous minerals, anorthite, augite and quartz, along with secondary minerals chabazite (*i.e.*, zeolite group) and smectite (*i.e.*, clay group). The analysis indicates that, other than small fluctuations in the anorthite and augite proportion, the mineralogical assemblage remains essentially stable up to 130 °C. The fraction of smectite identified in the samples decreases by ~6% following treatment to 185 °C and is mostly absent beyond 400 °C (Table 1). Analysis of the X-ray diffractograms show that the d(060) peak for unaltered surficial material is at 1.535 Å, whist the d(001) peak expands from 15 Å to 16.2 Å upon glycolation and collapses to 10 Å after dwelling at 400 °C for 12 hours, typical of saponite (Supplementary Figure 1).

XRD analysis of the subsurface hyaloclastite from Lévy et al., (2018) highlights that the smectite transitions from saponite in the surficial and shallow hyaloclastites, to interlayered saponite-chlorite in the deeper (556 m and 732 m) hyaloclastites.

Table 1. Primary mineralogy identified by X-ray diffraction analysis of hyaloclastite that has experienced different thermal treatment temperatures. Note that the reduction in the smectite proportion causes the relative proportions of the other components to increase and that the presence of sideromelane is not quantified nor included in this analysis.

Temperature experienced:	20 °C	130 °C	185 °C	400 °C	600 °C
Anorthite (%)	52	59	60	63	73
Augite (%)	17	13	18	25	17
Chabazite (%)	8	8	7	5	7
Quartz (%)	3	2	2	6	3
Smectite (%)	19	18	13	Trace	Trace
Total (%)	99	100	100	99	100

Petrographic analysis provides a textural counterpart to the quantitative mineralogical XRD. Thin section analysis, using both optical microscopy and scanning electron microscopy reveals the highly variable nature of hyaloclastite (Fig. 3). In particular, we note significant textural heterogeneity in terms of glass distribution and geometry, crystal fraction and size, and pore space distribution (Fig. 3). The pore space is shown to be predominantly hosted in the matrix in both as-collected and TT samples (Fig. 3b, r), with additional, closed porosity hosted within the highly variable vesicular glass clasts (Fig. 3j). Textural examination of the thin sections for the as-collected material shows a low quantity of intra-mineral micro-fractures within the phenocrysts and glass (Fig. 3b). A qualitative inspection of the TT sample thin sections found a comparable number of intra-mineral micro-fractures. Given the material heterogeneity we do not quantify this further, finding that material characterisation which examines porosity and permeability before and after TT on the same sample to be a more robust measure of sample evolution with TT. Thin section analysis also offers no evidence of reaction rims around crystals or of sintering textures, such as particle necking during agglutination occurring during TT (Fig. 3). Changes in the abundance of constituent phases as a result of TT are revealed by QEMSCAN (Table 2, Fig. 3). Changes in crystallinity are not recorded in the QEMSCAN maps and so the dissociation of smectite is not quantified; however, the textural evolution highlights that porosity increase is dominated by changes in the matrix, which we associate with a reduction in smectite revealed by XRD (from ~19 % to trace content at TT >400 °C, Table 1). Loss of smectite with temperature results in an irregular desiccated texture, distinct from a fractured surface due to its

345 smoother edges and globular distribution (Fig. 3b, r), causing the matrix to transition from a
346 continuous, pervasive network (Fig. 3c, g) to discrete patches with increasing TT temperature,
347 particularly in the 400 °C and 600 °C samples (Fig. 3o, s).

348 Table 2. Mineralogy for as-collected and for each treatment temperature quantified from the
349 QEMSCAN image analysis at 20 µm resolution (see Supplementary Figures 2 - 7). Note that changes to
350 mineral structure, such as dissolution, are not captured by QEMSCAN. Values are normalised by the
351 background (pore space) of each image.

Temperature experienced:	20 °C	130 °C	185 °C	400 °C	600 °C
Glass (%)	53.8	51.4	53.0	57.9	57.6
Smectite [Fe Mg] (%)	26.8	26.3	23.6	22.0	23.4
Zeolite (%)	8.8	9.2	8.2	8.0	8.3
Anorthite (%)	6.0	8.8	11.8	8.7	6.9
Augite (%)	2.6	2.6	2.1	2.5	2.3
Quartz (%)	0.3	0.3	0.3	0.3	0.4
Actinolite (%)	0.3	0.3	0.2	0.2	0.1
Others (%)	1.2	1.0	0.7	0.2	0.6
Unclassified (%)	0.2	0.1	0.2	0.2	0.4
Total (%)	100	100	100	100	100

352

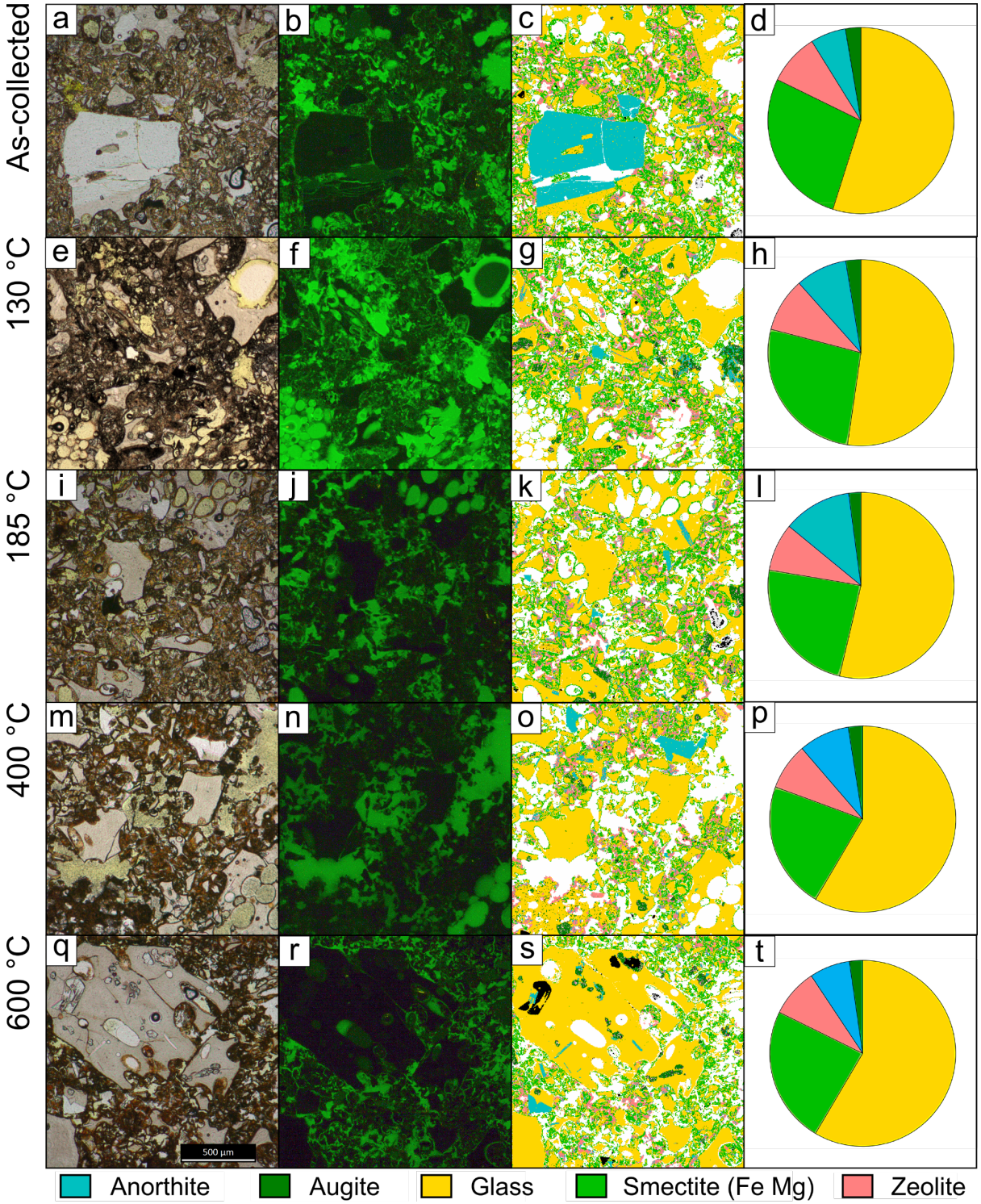

353

354 Figure 3 – Petrographic analysis for as-collected and TT samples. As-collected images are presented in
355 a – d; 130 °C TT images in e – h; 185 °C TT images in I – l; 400 °C TT images in m – p; and 600 °C TT
356 images in q – t, each image shows 1.5 mm^2. Plane polarised light images are displayed in column 1
357 (Supplementary Figure 2 shows an annotated example of the petrographic images); ultraviolet images
358 in reflected light of samples impregnated by fluorescent epoxy highlight porosity in column 2;
359 QEMSCAN mineralogy maps at 4 µm resolution in column 3 highlight mineral distribution; and

quantified mineralogy pie-charts from 20 µm resolution QEMSCAN maps in column 4 (images are shown in Supplementary Figures 3-6).

3.4 Thermally-induced Changes in Porosity and Permeability

The evolution of mass during thermal treatment is reported for the 26 mm by 52 mm samples in order to explore the impact of material heterogeneity, discussed in section 3.3, on mass loss (indicated by thermal analysis in section 3.1). Sample mass change in the surface cores is positively correlated with the TT (Fig. 4a). The samples cored from the as-collected material show a large degree of heterogeneity in the material properties despite being sourced from a single block ~40 cm in length. This hyaloclastite heterogeneity corresponds to substantial scatter in the porosity – gas permeability relationship (Fig. 4b). However, the effect of this scatter can be accounted for and removed from the TT data by normalising the porosity change against the initial porosity of the corresponding core prior to TT, ϕ_I:

$$\bar{\phi} = -\frac{\phi_I - \phi_P}{1 - \phi_I} \qquad \text{Eq. 4}$$

where ϕ_P is the post thermal-treatment porosity; similarly, the resultant permeability changes are normalised by dividing the post thermal-treatment sample permeability with the original sample permeability (Fig. 4c). The normalised plot shows that the permeability and porosity changes of all samples increase with TT (Fig. 4c).

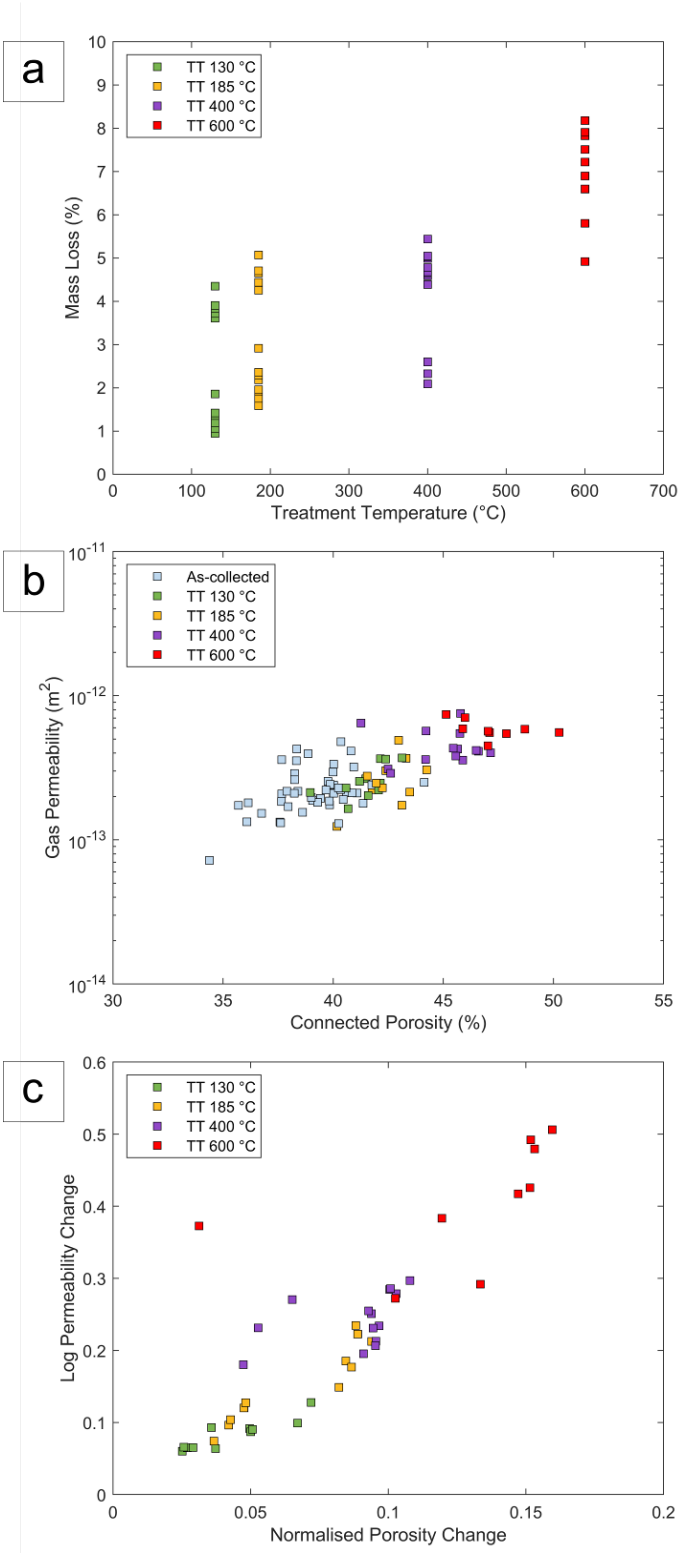

Figure 4 – Influence of TT on mass, porosity and permeability. a. Percentage mass change induced by thermal treatment for each 26 mm by 52 mm core, showing increasing mass reduction up to temperatures of 600°C; b. Increasing porosity - gas permeability of as-collected and post-treatment samples as the treatment temperature is increased; c. Normalised porosity and gas permeability

change from the as collected materials, showing a linear permeability change with increased normalised porosity change.

The water permeability of the hyaloclastite measured in the hydrostatic cell shows a negative correlation with effective pressure (Fig. 5a; Supplementary Table 1) as the permeable pathways are constricted by pore space closure (Fig. 5b). Again, the samples exhibit a large degree of scatter in permeability for all TTs, that is independent of the mass change induced by TT. The as-collected samples as well as those TT to 130 °C, and to an extent 185 °C, show a moderate-to-large drop in permeability above 17.5 MPa that is not observed in the 400 and 600 °C TT samples. These effective pressure thresholds are also observed in the porosity evolution plot (Fig. 5b), which shows a transition from low to high densification with effective pressure across these values. The samples that have been TT to higher temperatures exhibit contrasting evolution of permeability and porosity with effective pressure.

In these cases, the permeability of samples does not change significantly with effective pressure (Fig. 5a), whilst the porosity shuts linearly with effective pressure (Fig. 5b); The exception to this behaviour is for one sample (thermally treated to 400 °C) which shows an increase in permeability between 7.5 and 17.5 MPa (Fig. 5a); interestingly, this sample was accompanied by almost no porosity decrease between 17.5 and 23.5 MPa (Fig. 5b).

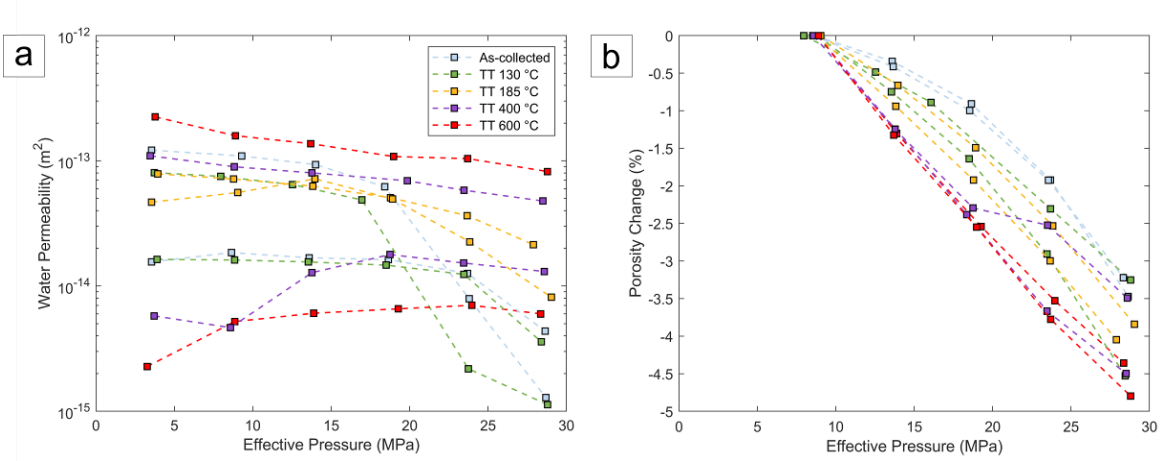

Figure 5 – The effect of loading on permeability and porosity. a. Water permeability evolution against effective pressure. Samples exhibit a large range of responses and degree of scatter for a given TT; b. Pore space collapse associated with increased effective pressure. Change in porosity is measured from ~8.5 effective pressure.

3.5 Thermally-induced Impacts on Strength

Uniaxial testing was used to constrain the behaviour of samples under compressive loading (Fig. 6a). The data show typical stress-strain relationships, such as documented in Heap et al. (2014a),

transitioning from an initial concave-upward segment, to being quasi-linear, followed by a concave-downward segment. In terms of absolute strain, the beginning and end of the quasi-linear segments are not correlated with treatment temperature; however, the average length of the linear portion decreases from 0.0034 - 0.0037 in the as-collected, 130 and 185 °C samples, to between 0.0021 - 0.0023 in the 400 and 600 °C samples. As the 400 and 600 °C samples experience more strain prior to failure than the as-collected and lower temperature samples, the shortening of the linear portion also corresponds to a significantly smaller proportion of the total stress-strain curve. The average gradient of the linear segment, which is associated with rock elasticity and is used to calculate the Young's modulus (Fig. 7d), also decreases with temperature beyond 400 °C, from between ~1300 and 1560 for the as-collected, 130 and 185 °C samples, to between ~700 and 1070 for the 400 and 600 °C samples. The data show that the as-collected, surficial hyaloclastites exhibit a range of compressive strength from 8 to 10 MPa (Fig. 6a). Upon thermal treatment to 130 and 185 °C, we observe no systematic changes in the sample strength, although the data shows wider scatter (Fig. 6a), whilst samples thermally treated to 400 and 600 °C weaken to between 4.2 and 6.8 MPa (Fig. 6a).

Triaxial testing was used to constrain the behaviour of the hyaloclastite at a confining pressure of 5 MPa (Fig. 6b), which is representative of ~300 m depth in the geothermal reservoir, assuming nominal rock and water densities of 2500 $Kg.m^{-3}$ and 800 $Kg.m^{-3}$, respectively (after Scott et al., 2019). Under such a confinement, the compressive strength of the as-collected hyaloclastite is ~30 MPa, exhibiting a small stress drop upon rupture. Following thermal treatment at 130 and 185 °C, hyaloclastite exhibits a moderate strength decrease of up to 3.3 and 7.2 MPa, respectively; yet, the stress-strain curves show systematic reductions in the stress drop upon rupture. Hyaloclastite subjected to higher temperatures of 400 or 600 °C reveal contrasting behaviour in which samples tend to yield at lower differential stress, beginning to flow upon strain (Fig. 6b); the one exception to this is the strongest sample, treated at 400 °C, which was texturally comparable to the other TT samples, and yet shows mechanical behaviour similar to samples subjected to lower temperatures. Thus, thermal debilitation slightly weakens hyaloclastite and promotes a shift towards a ductile regime (Figure 6b; Supplementary Table 2).

Brazilian tests were used to quantify the UTS of hyaloclastite (Fig. 6c; Supplementary Table 3). The as-collected hyaloclastite shows a near linear stress loading curve and a UTS of 1.5 MPa. Upon thermal treatment to 130, 185 and 400 °C, we note a systematic weakening trend down to 0.6 MPa. Hyaloclastite subjected to the higher 600 °C temperature do not weaken further but rather undergo more compaction prior to failure.

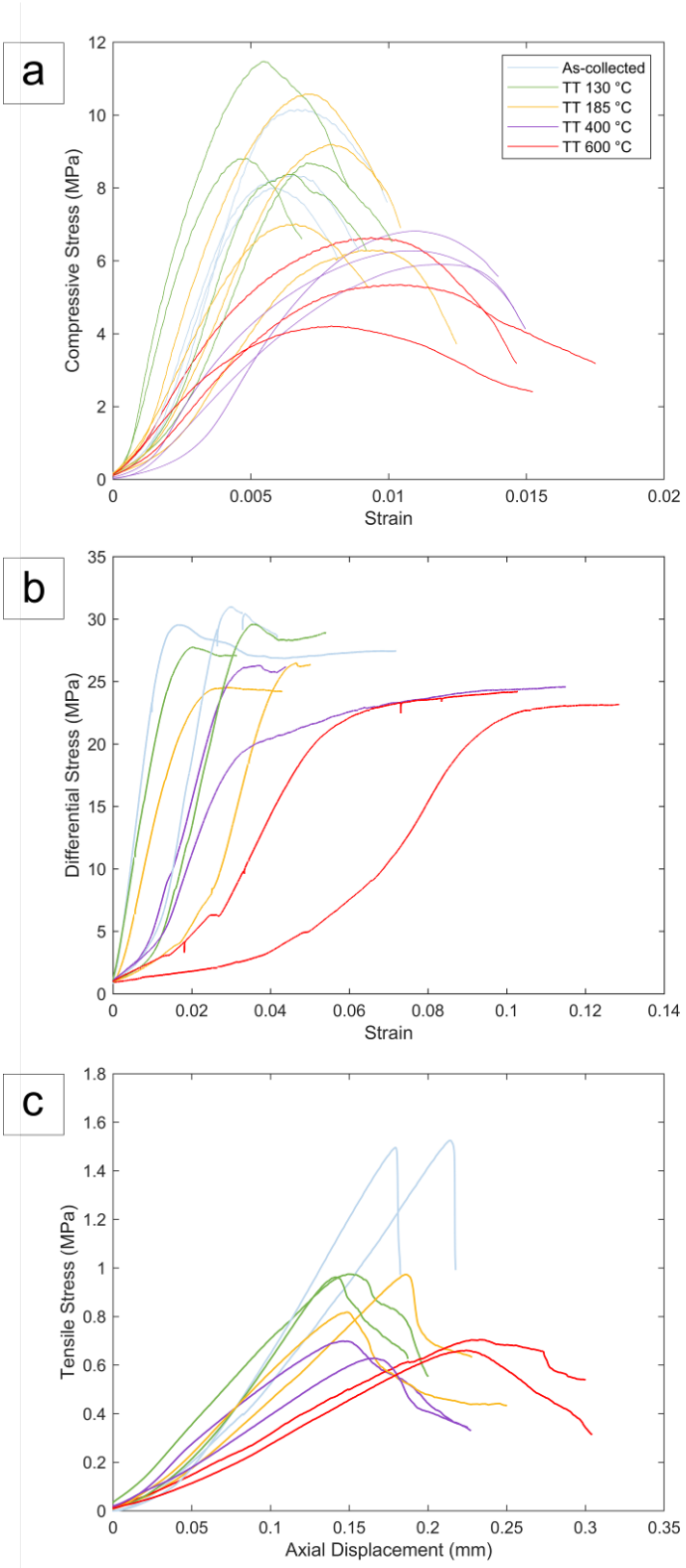

439

440 Figure 6 – The impact of TT on strength. a. UCS curves at 10^{-5} s^{-1} strain rate; b. TXL curves at 10^{-5} s^{-1}
441 strain rate; c. UTS curves, using the Brazilian disc method, at 10^{-4} s^{-1} diametric equivalent strain rate.
442 For increased TT, all strength test types display a weakening trend and an increased accommodation
443 of strain prior to failure (Additional tensile strength curves are shown in Supplementary Figure 8).

The peak strengths from UCS, TXL and UTS curves show a decreasing trend with porosity and TT (Fig. 7a). Analysis of the UCS (Fig. 7b), UTS (Fig. 7c) and Young's modulus data (Fig. 7d) show they follow trends published for igneous rocks. The Young's moduli obtained from the uniaxial (Fig. 6a) and triaxial (Fig. 6b) strength tests reveal a negative correlation with the connected porosity of samples, imparted by thermal treatment. The Young's moduli obtained during uniaxial tests are generally lower than the equivalent triaxial results for a given porosity (Fig. 7d).

The data presented here highlights the substantial impact of thermal treatment on the mineralogical, physical and mechanical properties of altered reservoir rocks as present in active geothermal systems. Notably, increasing temperature results in lower smectite contents, higher porosity and permeability and lower compressive and tensile strengths.

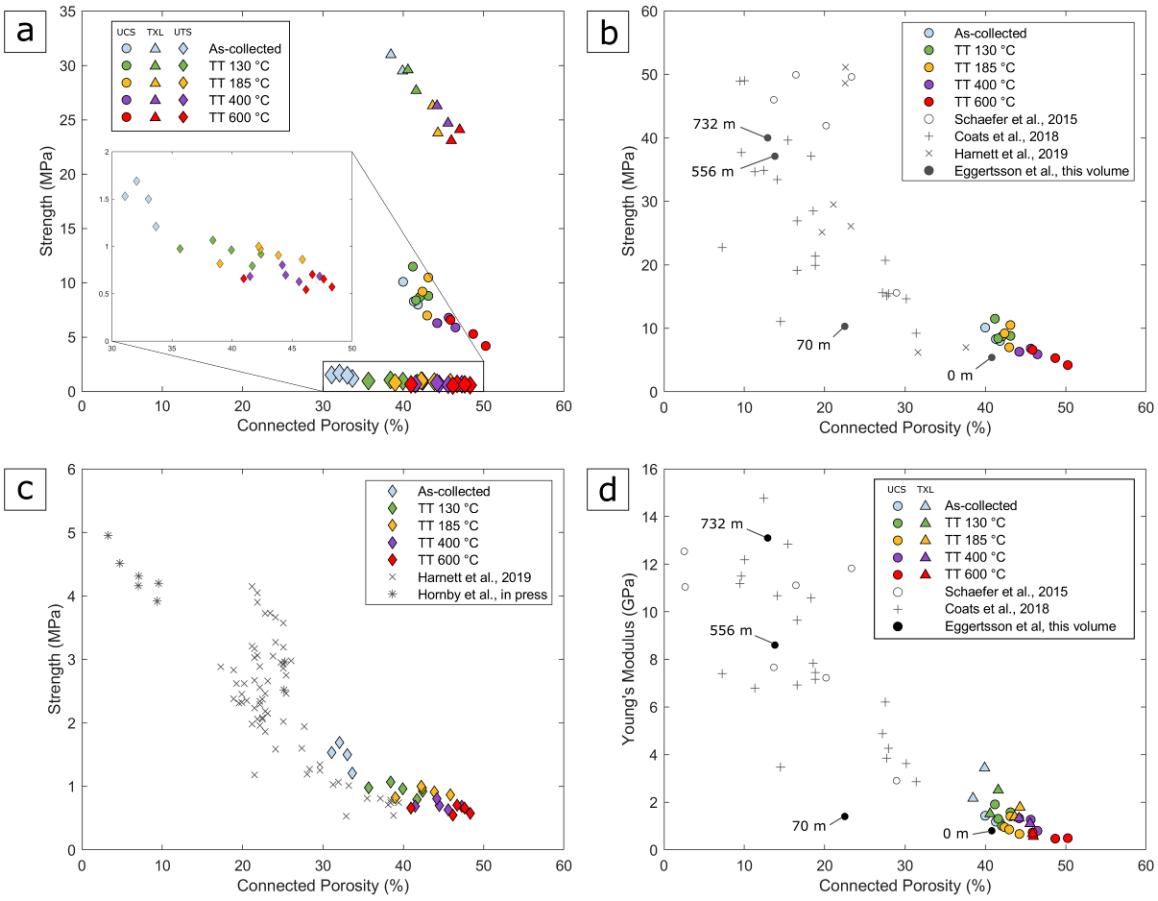

Figure 7 – Porosity control on UCS, TXL, UTS, and Young's modulus. a. Comparison of UCS, TXL and UTS peak strength of hyaloclastite for each treatment temperature. All strength test types show weakening associated with increased TT and porosity; b. UCS results follow the general trend for igneous rocks, with TT decreasing strength proportional to the porosity increase. However, TT increases porosity, whilst hyaloclastite densifies and strengthens with depth (values show depth of sampling; Eggertsson et al., this volume); c. UTS results, regardless of TT, also fall within the general

trend for igneous rocks; d. Young's modulus from UCS and TXL tests follow the general trend for igneous rocks (values show depth of sampling; Eggertsson et al., this volume).

4. Interpretation and Discussion

4.1 Application of Laboratory Results to the Field

The investigation on the thermal stability of hyaloclastite present up to 1300 m depth in the shallow geothermal reservoir within Krafla caldera provides important constraints on the properties of a common reservoir rock. However, due to the physically and mineralogically heterogeneous nature of hyaloclastite, studies at a laboratory scale (*e.g.*, Eggertsson et al., 2018; Franzson et al., 2010) are challenging to apply to field scales. The variations noted in the mineralogical assemblage of the surficial hyaloclastite studied here (Tables 1 and 2) are likely due to the physically and mineralogically variable source volcaniclastic components, despite being prepared from a single 40 cm block. Influence of this heterogeneity continuously transpires in the physical and mechanical characterisation of both the as-collected and TT samples, particularly highlighted by the contrasting permeability behaviour in Figure 5a. Heterogeneity at the field scale may be markedly greater due to sorting and componentry (Schopka et al., 2006), and the degree of alteration, particularly between hyaloclastites exposed to different fluid chemistry (Kristmannsdóttir, 1979). Therefore, the data and trends of thermal treatment are most applicable to smectite-bearing hyaloclastite exposed to meteoric-sourced fluids, such as at Krafla. Here we interpret the influence of thermal treatment on the physical and mechanical properties of surficial hyaloclastite and compare the resultant properties with those obtained from cores sampled from depth.

4.2 Impact of Temperature on the Mineralogical Assemblage of Hyaloclastite

Thermally treating hyaloclastite results in mass loss (Fig. 2a), which can be used as a proxy for water loss in hydrous clays (Bishop et al., 1994; Milliken and Mustard, 2005; Yen et al., 1998). However, it is important to note that phyllosilicates, such as smectite, comprise a group of highly variable minerals that have distinct dehydration and dehydroxylation temperatures (Yariv et al., 1992). The reduction in the d(001) spacing in the XRD data (Supplementary Figure 1) is linked to the dissociation of the palagonite matrix resulting from smectite dehydration (Table 1). In detail, gylcolation firstly causes the d(001) peak to increase to 16.2 Å, as ethylene glycol replaces water in the interlayer space (*e.g.,* Mosser-Ruck et al., 2005); subsequent heating to 400 °C for 12 hours drives ethylene glycol and water out of the interlayer space, decreasing the d(001) peak to 10 Å (*e.g.,* Shirozu et al., 1975). Therefore, the reduction in smectite quantity with temperature is more accurately a case of progressive alteration (dehydration), which ultimately damages the crystal structure and reduces the effectiveness of the diffraction process. This produces smaller peaks in the diffractogram, which are

interpreted as a lower mineral quantity; a similar reduction in smectite is not observed in the QEMSCAN data (Table 2) as only chemistry is monitored, and not crystal structure. The low-temperature (< 200 °C) devolatilisation reactions identified in the TGA-DSC data (Fig. 2a, b) correlate well with the clay-separated XRD results (Supplementary Figure 1). The endothermic DSC peaks at 130 °C and 185 °C (Fig. 2b) are encompassed within the 100 – 200 °C dehydration window expected for saponite (Malek et al., 1997) and are likely due to the loss of sorbed water and interlayer water (Shirozu et al., 1975). Saponite commonly precipitates from hydrothermal fluids found at depth (Alfredsson et al., 2013; Gysi and Stefánsson, 2012) and has been previously identified in cores from the Krafla geothermal reservoir (Kristmannsdóttir, 1979). The subsurface samples have less prominent saponite dehydration peaks due to a combination of lower saponite-chlorite ratios and the higher *in-situ* temperatures potentially causing partial dehydration prior to measurement (Lévy et al., 2018). The ability of smectite to rehydrate is dependent upon temperature, cation size and saturation state (Kawano and Tomita, 1991). Under many conditions saponite is able to fully or partially rehydrate (Russell and Farmer, 1964), suggesting the impacts discussed here may be partially reversible.

The 525 – 560 °C endothermic peaks identified in the 556-m and 732-m samples (Fig. 2b) are indicative of chlorite dehydroxylation from interstratified saponite-chlorite (Shirozu et al., 1975), resulting in a second higher temperature mass loss response (Fig. 2a). The endothermic peak and associated mass loss are greater within the 732-m sample, suggesting it has a lower saponite-chlorite ratio than the 556-m sample. The combined saponite-chlorite content at Krafla increases erratically from 19% at the surface, to ~50% at depth, not including glass content (Lévy et al., 2018), suggesting thermally-induced devolatilisation reactions at depth may be more impactful. However, note that all of the TGA-DSC measurements were performed under near-atmospheric pressure conditions, and that increased pressure from the subsurface may suppress dehydration and dehydroxylation to higher temperatures (Vidal and Dubacq, 2009), such that the temperatures for reactions presented here are potentially conservative compared to those occurring in-situ. Following the devolatilisation of the phyllosilicates, the bulk rock density increases due to the residual minerals emitting light elements; upon compaction, this may impact the physical and mechanical rock properties.

4.3 Impact of Temperature on the Thermal Expansivity of Hyaloclastite

In addition to mass loss, the thermal treatment of hyaloclastite also results in direct volume change as the palagonite phyllosilicate phases are prone to swelling at low temperatures and subsequently collapse following thermally-induced dehydration and dehydroxylation (*e.g.*, >500 °C; Fig. 2d). However, identifying the swelling properties of individual components in a porous polymineralic rock is challenging due to the potential for overlapping responses and the possibility of accommodating expansion into the pore space (Cooper and Simmons, 1977). In the surface samples, the impact of

saponite dehydration in the thermo-mechanical data (Fig. 2d) is subtle, causing a minor compaction of the bulk rock, followed by significant compaction correlating with the chlorite dehydroxylation temperature. This suggests that hyaloclastite retains structural integrity throughout saponite dehydration whilst a higher temperature reaction correlated to chlorite dehydroxylation causes a partial loss of cohesion between the palagonite matrix and the supported clasts. The similar, more distinct collapse in the relatively chlorite-rich 732-m sample at 575 °C correlates well with the endothermic peak at 560 °C and the mass loss identified between 515 °C and 615 °C (Fig. 2a, b). However, the 556-m subsurface sample has lower saponite-chlorite ratios and does not exhibit this collapse, instead the response shows limited thermal expansion throughout the heating profile. Thus, we find that hyaloclastites with thermally-stable mineralogical assemblage expand with temperature, whereas unstable assemblages may breakdown and cause contraction, as exemplified by the thermal treatment of surficial hyaloclastites (Fig. 2d). The thermal expansion responses measured under near-atmospheric pressure conditions, and any damage attributed to them, may be pushed to higher temperatures under the increased pressure conditions associated with burial, as dehydration is suppressed (Vidal and Dubacq, 2009). However, without a change in temperature, an increase in pressure alone does not result in smectite dehydration (*e.g.*, Carniel et al., 2014).

The occurrence of substantial acceleration in thermal expansion above 640 °C from the 70-m samples (Fig. 2d), coincided with vesiculation of glass clasts in the experimental products; this was not reproduced in samples from other depths, despite the abundance of glass in all samples (Fig. 3). In detail, thermal expansivity started to accelerate around 600 °C, following a moderate endothermic peak (Fig. 2b), associated with crossing of the glass transition for hydrated basaltic glass (Giordano et al., 2008; Robert et al., 2014), expected in shallow, water-rich environments (Cerling et al., 1985). Beyond this temperature, structural relaxation of the stress enabled water exsolution and increased vesiculation that sustained the heat absorption leading to a prolonged endothermic plateau (Fig. 2d), as the samples rapidly expanded (Fig. 2b).

4.4 Impact of Temperature on the Porosity and Permeability of Hyaloclastite

The mass loss associated with the dehydration/dehydroxylation of the phyllosilicate phases during thermal treatment of hyaloclastite is also responsible for the increase in porosity and permeability displayed in Figure 4. Temperature increase can strongly impact the physical attributes for fluid storage capacity and flow, as the basal spacing of palagonite decreases upon devolatilisation, causing densification and generating intrinsically connected micro-pores (*e.g.*, Kolaříková et al., 2005). In detail, the amount and ratio of saponite-chlorite available for reaction provides a first order control on the maximum extent of porosity possibly created by excursion to high temperature. As such, the time-dependent crystallisation of sideromelane to palagonite (Drief and Schiffman, 2004) suggests

562 that older hyaloclastite units, which can contain more phyllosilicates, are more susceptible to
563 temperature increases and the resultant enhancements to the porous permeable network. Thus, the
564 lithology-specific initial glass chemistry, hydrothermal fluid chemistry, and pressure-temperature
565 conditions will therefore impact the potential for temperature-induced mineralogical and physical
566 alteration that regulate the evolution of the storage capacity and permeability of a reservoir subjected
567 to thermal fluctuations. In addition, the reservoir fluid properties will impact upon the hydration state
568 of the phyllosilicate minerals; the increased scatter from water permeability (Fig. 5a) to gas
569 permeability (Fig. 4b) is likely a result of interaction between the pore fluid and the permeable
570 network.

571 At the sample scale, the lack of additional fractures in the TT samples suggests that
572 dehydration/dehydroxylation is the primary mechanism responsible for porosity and permeability
573 gain. Whilst cracking due to thermal stresses during heating and cooling have been shown to impart
574 changes in the physical properties of some rocks, we advance that thermally generated-cracks may
575 not necessarily accumulate in hyaloclastite. Thermal cracking has been ascribed to the generation of
576 stresses resulting from: 1. A mismatch in thermal expansion or contraction between minerals; 2.
577 Thermal expansion anisotropy within a mineral and; 3. Thermal gradients across a sample (e.g., Richter
578 and Simmons, 1974; Yong and Wang, 1980). Hyaloclastites are fragmental rocks with variable degrees
579 of cohesion arising from the presence of palagonite, so thermal stressing is expected to cause minimal
580 damage in hyaloclastite as mineral expansion is in-part buffered by palagonite, which is weaker than
581 typical volcanic minerals, and due to the abundant and ubiquitous pore space that accommodates
582 expansion without stress development. Eggertsson et al., (2018) showed that thermal stimulation may
583 avoid fracture genesis and result in negligible permeability change, independent of cooling rate, if the
584 thermal stress is accommodated by an existing porous network, such as present in these samples (Fig.
585 2b). We also note no evidence of intra-mineral thermal cracking induced by anisotropic expansion.
586 However, it is possible that inter-phenocryst/glass fragment micro-fracturing occurred, as noted in
587 hyaloclastite quenched from 350 °C (Siratovich et al., 2011), but that textural evidence was
588 subsequently overprinted by phyllosilicate dissolution. Thermal micro-fractures are often non-
589 pervasive in nature (e.g., Browning et al., 2016; Heap et al., 2012), suggesting the limited contribution
590 they provide to permeability is unable to account for the permeability evolution revealed in this study.
591 Deformation-induced macro-fractures may induce more substantial permeability increase (Heap and
592 Kennedy, 2016; Lamur et al., 2017), yet such damage is not imparted by thermal treatment alone.
593 However, the impact of thermal fracturing on the broad range of volcanic lithologies is yet to be well
594 constrained, as discussed in Heap et al., (2014a), and very few studies focus on highly altered material
595 and the impact of pressure on thermal stimulation (*e.g.,* Mordensky et al., 2019).

A further measure of changing material properties as a response to TT can be the sensitivity of materials to effective pressure; water permeability shows a negative correlation with effective pressure as porosity is closed (Fig. 5). The as-collected samples as well as those TT to 130 °C, and to 185 °C, show a significant drop in porosity and permeability during confinement to effective pressures above 17.5 MPa that is not observed in the 400 and 600 °C TT samples. The samples that have been TT to higher temperatures exhibit contrasting evolution of permeability and porosity with effective pressure, where porosity decreases linearly and more significantly than the lower TT samples, but permeability is not as sensitive to increasing effective pressure; suggesting that the porous network remains highly connected even as effective pressure is increased. There is one exception (thermally treated to 400 °C) which shows an increase in permeability with increasing effective pressure, and a less significant reduction in porosity, this could be a result of irreversible compaction in the sample whereby connected pore space was generated, yet we observed no textural evidence for this.

4.5 Impact of Temperature on the Mechanical Properties of Hyaloclastite

The addition of thermal stress can also impact the resultant mechanical properties of hyaloclastite. In particular, pressure increase causes a relatively abrupt reduction in pore space and permeability within the as-collected hyaloclastite and the samples thermally treated to 130 °C (Fig. 5). This transition from elastic to inelastic compaction upon loading is termed P* (Zhang et al., 1990). Beyond P*, compaction and grain crushing lead to a loss of pore space available for fluid flow (Bedford et al., 2018; Eggertsson et al., 2018; Heap et al., 2015). That samples thermally treated to 185 °C exhibit a poorly defined P*, and higher temperature samples develop no distinct P*, suggests that thermal treatment promotes a style of compaction that has limited impact on permeability, despite higher rates of porosity loss (Fig. 5b).

The devolatilisation of the palagonite matrix results in a weakening of the rock, both in tension and compression, where the UCS is 6 – 10 times greater than the UTS (Fig. 7a). The UTS of hyaloclastite decreased with TT, and following treatment at 600 °C, lost coherence and underwent more deformation before rupture (Fig. 6c). The mode of deformation evolves similarly in compression, as noted by the onset of dilation occurring at lower stress and the accommodation of more substantial strain hardening prior to failure (Fig. 6a), concordant with lower Young's modulus upon increasing treatment temperature (Fig. 7d). Deformation under an effective pressure of 5 MPa accentuated the distinction between low TT (≤185 °C) and high TT (≥400 °C) hyaloclastite as they macroscopically behaved in a brittle and ductile manner, respectively (Fig. 6b).

The resultant strengths measured in all test types display a porosity control, irrespective of the stress field experienced (Fig. 7a), that follows the common porosity-strength trend (Fig. 7b and 7c) for a range of igneous rock types, regardless of TT (Coats et al., 2018; Eggertsson et al., this volume.; Harnett et al., 2019; Hornby et al., 2019; Schaefer et al., 2015). The treatment temperature has a strong impact on porosity (Fig. 4c), thereby further influencing mechanical compaction; however, comparison with strength and Young's modulus data collected from subsurface samples (Eggertsson et al, this volume) shows that temperature alone cannot explain the mechanical changes occurring within the reservoir, instilling the roles of compaction and alteration on strength changes. In part, this is due to the opposing influences of temperature and compaction on porosity; however, in concert, increased temperature will create additional pore space that may enable more complete compaction and densification to occur at depth (Eggertsson et al, this volume). The change in style, from a dominantly brittle to ductile failure, may be explained by a change in geometry of the pore space (*e.g.*, Fig. 3b vs 3r), as dehydration increases the connectivity and irregularity of the desiccated pore network (Bubeck et al., 2017). The influence of porosity in controlling sample strength can be further assessed using micro-mechanical modelling such as the pore-emanated crack model developed by Sammis and Ashby, (1986) and analytically modified by Zhu et al. (2010) to derive the UCS, σ_{UCS}:

$$\sigma_{UCS} = \frac{1.325}{\phi^{0.414}} \frac{K_{IC}}{\sqrt{\pi r}} \qquad \text{Eq. 5}$$

The strength is dependent upon the fracture toughness (or critical stress intensity factor), K_{IC} , the porosity (ϕ) and pore size (r). This model was demonstrated to successfully approximate the UCS of limestone (Zhu et al., 2010) and porous glass sintered in the laboratory (Vasseur et al., 2013), but show arguable efficiency to approximate the strength of heterogeneous, coherent volcanic rocks, owing to their common abundance of micro-fractures (Coats et al., 2018; Heap et al., 2014a). Here, the UCS values decrease as porosity increases with TT (Fig. 8), suggesting that $\frac{K_{IC}}{\sqrt{\pi r}}$ would decrease from ~5 MPa down to ~3 MPa. Assuming K_{IC} remains constant within a single lithology (even upon smectite hydration) the analysis would suggest that the reduction in strength and $\frac{K_{IC}}{\sqrt{\pi r}}$ may be the result of pore creation and widening, as suggested by Heap et al. (2014a) when evaluating the mechanisms underlying thermally-induced rock weakening. However, the applicability of the pore-emanated crack model to hyaloclastite is questionable as the pore space is highly irregular and rock failure is promoted by increasingly more pervasive fracture architecture in thermally treated hyaloclastites.

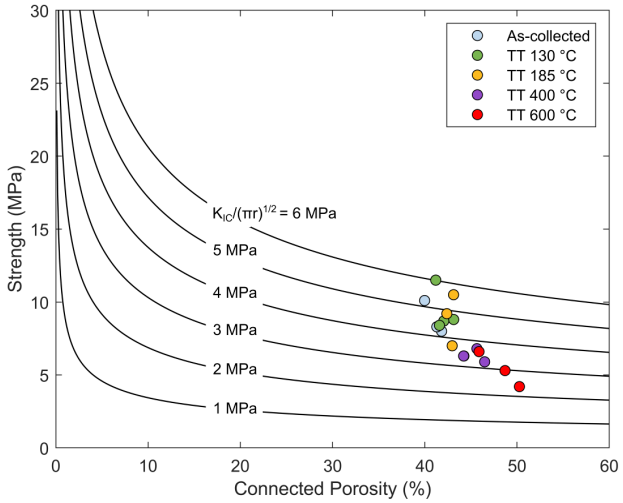

Figure 8. UCS measurements compared against the pore-emanated crack model suggest an increase in porosity and pore-widening results in weakening.

4.6 Implications for Hyaloclastite-bearing Geothermal Reservoirs

The temperatures investigated here cover the range of conditions hyaloclastite generally encounters in the shallow geothermal reservoir at Krafla (Bodvarsson et al., 1984) and encompass several important mineral transitions within the palagonite matrix. The transition from smectite to chlorite is common in hyaloclastite-bearing geothermal regions and is predominately controlled by temperature, assuming similar fluid chemistry (Kristmannsdóttir, 1979). Saponite is dominant below 200 °C, transitions to saponite-chlorite interlayers between 200 – 240 °C and is fully replaced with chlorite beyond 240 °C (Kristmannsdóttir, 1979). Therefore, these results provide a first order approximation of the changes occurring in hyaloclastite during burial and regional heating. Well and core logging at Krafla suggests that the deepest hyaloclastite units at 1300 m naturally experience temperatures of approximately 320 °C (Fridleifsson et al., 2006) and thus would have been subjected to the full range of transitions. However, as the temperature profile is spatially variable across the field, the depth of mineral transitions range over several hundred metres (Fridleifsson et al., 2006).

Some geothermal regions, such as Krafla, are also host to magmatic intrusions that can transfer heat to their host rock, inducing much greater localised temperature changes (*e.g.*, Schauroth et al., 2016). Similarly, harnessing of very hot fluids, as experienced during flow testing of a 2100 m deep, near-magma borehole during IDDP-1 (Mortensen et al., 2014), resulted in fluids up to 550 °C reaching the wellhead. Thus, a shallow magmatic intrusion or superheated/supercritical fluid ingress during flow testing can alter the mineralogical, physical and mechanical properties of shallow hyaloclastite, common in conventional geothermal reservoirs. This may promote more efficient fluid flow in geothermal fields; yet, fluid flow in clay-bearing rocks is partially controlled by the chemistry of the

681 fluids which can interact with the host (Kwon et al., 2004); thus the impact of fluid chemistry on fluid
682 flow is expected to decrease upon palagonite dissociation. Here, comparing the surficial hyaloclastite
683 with the hyaloclastites sampled from the reservoir, we find that the thermal-induced mass loss and
684 mineralogical distribution of the deep hyaloclastites cannot be explained by simple heating events, as
685 those performed in our experiments, but rather evoke the importance of pressure-temperature
686 history and chemistry in the hydrothermal system. For instance, the onset of saponite dehydration
687 may increase by several hundred degrees by increasing pressure to 30 MPa (Vidal and Dubacq, 2009),
688 such as through rock burial or glaciation, suggesting the physical and mechanical changes detailed
689 here may be shifted to higher temperatures for buried samples. Additionally, the impact of pore fluid
690 pressure may suppress dehydration reactions to higher temperatures than recorded in the dry
691 measurements presented here (de Siqueira et al., 1999). As such, the interplay between temperature
692 and pressure produces a complex relationship with the resultant mineralogical, physical and
693 mechanical properties. Geothermal regimes with low effective pressure and high temperature, such
694 as the shallow subsurface, may exhibit a positive correlation between the temperature experienced
695 and the resultant porosity and permeability, whilst in a deeper high-pressure environment, the
696 breakdown from thermal fluctuations, if any, may promote compaction.

697 Anthropogenic-induced compaction may possibly occur due to the extraction of geothermal fluids
698 inducing a reduction in the reservoir pore pressure (Segall and Fitzgerald, 1998); this would increase
699 the effective pressure and subsequently raise the depth threshold of compaction (*e.g.*, Farquharson
700 et al., 2016), locally altering the dominant permeability regime. Porosity change associated with
701 temperature fluctuations may also influence the depth threshold of compaction. Similarly, a
702 temperature reduction caused by fluid extraction may result in rehydration and swelling due to the
703 potentially reversible nature of smectite dehydration, thereby clogging fluid pathways.

704 ### 4.7 Implications for Magma Intrusions in Hyaloclastite

705 The intrusion of magma into hyaloclastite may result in complex intrusion-host rock interaction,
706 evolution and feedback, owing to variable degrees of devolatilisation and compaction. Initially, an
707 intrusion would bake the margin, promoting phyllosilicate devolatilisation that improves the porous
708 permeable network, allowing for efficient fluid flow; however, this may be accompanied by changes
709 in strength and a transition from brittle to ductile deformation, which may instead favour compaction
710 of the hyaloclastite along the magma boundary, causing a decrease in permeability (*e.g.*, Farquharson
711 et al., 2017) and compartmentalisation of fluid flow (*e.g.*, Senger et al., 2012). The construction versus
712 destruction of a permeable porous network may have crucial impacts for the evolution of shallow
713 magmatic systems. Firstly, the liberation of fluids from smectite and chlorite may, if trapped, locally
714 increase pore pressure and generate induced seismicity akin to hydraulic fracturing (Wang and Wong,

2003), and, in extreme cases, cause phreatic explosions, as seen at Viti crater, Krafla (*e.g.*, Mayer et al., 2015). Secondly, the volatiles liberated may promote magma hydration and increase the likelihood of explosive activity (*e.g.*, Zhang, 1999), or result in cooling and quenching of the magma. Thirdly, and similarly, margin compaction and shutting of the permeable network may limit magma outgassing, which again increases the likelihood of explosive volcanism. And finally, magma intrusion may result in viscous relaxation of sideromelane or melting of hyaloclastite, thus generating new magma, which may mix and interact with the intrusion. Thus the evolution and feedbacks between magma and hyaloclastite are likely to be very complex depending on the nature (*e.g.*, chemistry, temperature) and size of an intrusion, and on the state and properties of hyaloclastites. We suggest that further research should be undertaken to better understand these complex feedback systems and the implications for volcanic and geothermal processes.

5. Conclusion

In this study, we show that rock heterogeneity impacts the mineralogical, physical and mechanical properties of hyaloclastite, which are susceptible to thermal fluctuations experienced within geothermal fields. This is due to the devolatisation of the palagonite matrix, comprised of varying phyllosilicate minerals which are sourced from the tendency of metastable basaltic glass to crystallise and produce a smectite-dominant (*i.e.*, saponite) palagonite matrix in cool settings (<200 °C) and a chlorite-dominant matrix in hotter settings.

Thermal treatment of surficial hyaloclastite indicates that smectite dehydrates upon heating, with increased treatment temperature causing up to 10 wt.% mass loss at 700 °C. This dehydration, quantified at 130, 185, 400 and 600 °C, results in an enhanced porous permeable network, a decreased compressive and tensile strength, a decreased Young's modulus and a shift from brittle to ductile mode of deformation upon thermal treatment (≥400 °C), even at a moderate effective pressure of 5 MPa (as experienced at shallow depths in a geothermal system). We assess the impact of temperature on hyaloclastite sampled from boreholes at 70, 556, and 732 m depth in the reservoir, finding that the glass in the shallow rock may have been hydrated whereas the deeper rocks contain abundant chlorite, which dehydroxylates at ~560 °C.

The increased temperatures and pressures experienced in geothermal fields will reduce the hydration state of phyllosilicate minerals, causing weakening and potentially lowering the depth threshold for compaction. Such deformation in geothermal systems and areas surrounding magmatic bodies may result in the construction/destruction of fluid pathways and the compartmentalisation of reservoirs, possibly impacting on the progression of volcanic activity.

6. Acknowledgements

This study has been conducted as part of a PhD supported by the Natural Environment Research Council (NERC) EAO Doctoral Training Partnership that is funded by NERC, whose support is gratefully acknowledged. This research was further supported by Landsvirkjun National Power Company of Iceland and by Landsvirkjun's Energy Research fund, in addition to a Starting Grant from the European Research Council (ERC) to Y. Lavallée on Strain Localisation in Magma (SLiM, no. 306488) and an Early Career Fellowship of the Leverhulme Trust (ECR 2016-325) granted to J.E. Kendrick.

7. References

Alfredsson, H.A., Oelkers, E.H., Hardarsson, B.S., Franzson, H., Gunnlaugsson, E., Gislason, S.R., 2013. The geology and water chemistry of the Hellisheidi, SW-Iceland carbon storage site. Int. J. Greenh. Gas Control 12, 399–418. https://doi.org/10.1016/J.IJGGC.2012.11.019

Ármannsson, H., Fridriksson, T., Benjamínsson, J., Hauksson, T., 2013. History of Gas in Geothermal Fluids, Krafla, Northeast Iceland. Procedia Earth Planet. Sci. 7, 23–26. https://doi.org/10.1016/J.PROEPS.2013.03.192

Ármannsson, H., Gudmundsson, A., Steingr\'\imsson, B., 1987. Exploration and development of the Krafla geothermal area. Jökull 37, 13–30.

Axelsson, G., others, 2012. Temperature condition modelling for well IDDP-1 in Krafla, N-Iceland. 001251218.

Bedford, J.D., Faulkner, D.R., Leclère, H., Wheeler, J., 2018. High-resolution mapping of yield curve shape and evolution for porous rock: The effect of inelastic compaction on porous bassanite. J. Geophys. Res. Solid Earth 123, 1217–1234.

Berger, G., Schott, J., Loubet, M., 1987. Fundamental processes controlling the first stage of alteration of a basalt glass by seawater: an experimental study between 200° and 320°C. Earth Planet. Sci. Lett. 84, 431–445. https://doi.org/10.1016/0012-821X(87)90008-2

Bergh, S.G., Sigvaldason, G.E., 1991. Pleistocene mass-flow deposits of basaltic hyaloclastite on a shallow submarine shelf, South Iceland. Bull. Volcanol. 53, 597–611.

Bernabé, Y., Mok, U., Evans, B., 2003. Permeability-porosity relationships in rocks subjected to various evolution processes. Pure Appl. Geophys. 160, 937–960.

Bird, D.K., Schiffman, P., Elders, W.A., Williams, A.E., McDowell, S.D., 1984. Calc-silicate mineralization in active geothermal systems. Econ. Geol. 79, 671–695.

777 Bishop, J.L., Pieters, C.M., Edwards, J.O., 1994. Infrared spectroscopic analyses on the nature of water
778 in montmorillonite. Clays Clay Miner. 42, 702–716.

779 Bodvarsson, G.S., Benson, S.M., Sigurdsson, O., Stefansson, V., Eliasson, E.T., 1984. The Krafla
780 geothermal field, Iceland: 1. Analysis of well test data. Water Resour. Res. 20, 1515–1530.

781 Browning, J., Meredith, P., Gudmundsson, A., 2016. Cooling-dominated cracking in thermally stressed
782 volcanic rocks. Geophys. Res. Lett. 43, 8417–8425.

783 Bubeck, A., Walker, R.J., Healy, D., Dobbs, M., Holwell, D.A., 2017. Pore geometry as a control on rock
784 strength. Earth Planet. Sci. Lett. 457, 38–48.

785 Carniel, L.C., Conceição, R.V., Dani, N., Stefani, V.F., Balzaretti, N.M., dos Reis, R., 2014. Structural
786 changes of potassium-saturated smectite at high pressures and high temperatures: Application
787 for subduction zones. Appl. Clay Sci. 102, 164–171.

788 Cerling, T.E., Brown, F.H., Bowman, J.R., 1985. Low-temperature alteration of volcanic glass: hydration,
789 Na, K, 18O and Ar mobility. Chem. Geol. Isot. Geosci. Sect. 52, 281–293.

790 Clearwater, J., Azwar, L., Barnes, M., Wallis, I., Holt, R., 2015. Changes in injection well capacity during
791 testing and plant start-up at Ngatamariki. Changes 19, 25.

792 Coats, R., Kendrick, J.E., Wallace, P.A., Miwa, T., Hornby, A.J., Ashworth, J.D., Matsushima, T., Lavallée,
793 Y., 2018. Failure criteria for porous dome rocks and lavas: a study of Mt. Unzen, Japan. Solid Earth
794 9, 1299–1328.

795 Cooper, H.W., Simmons, G., 1977. The effect of cracks on the thermal expansion of rocks. Earth Planet.
796 Sci. Lett. 36, 404–412.

797 Davis, A.S., Clague, D.A., 2003. Hyaloclastite from Miocene seamounts offshore central California:
798 compositions, eruption styles, and depositional processes. Washingt. DC Am. Geophys. Union
799 Geophys. Monogr. Ser. 140, 129–142.

800 De Simone, S., Vilarrasa, V., Carrera, J., Alcolea, A., Meier, P., 2013. Thermal coupling may control
801 mechanical stability of geothermal reservoirs during cold water injection. Phys. Chem. Earth,
802 Parts A/B/C 64, 117–126.

803 de Siqueira, A. V, Lobban, C., Skipper, N.T., Williams, G.D., Soper, A.K., Done, R., Dreyer, J.W.,
804 Humphreys, R.J., Bones, J.A.R., 1999. The structure of pore fluids in swelling clays at elevated
805 pressures and temperatures. J. Phys. Condens. Matter 11, 9179.

806 Denton, J.S., Tuffen, H., Gilbert, J.S., Odling, N., 2009. The hydration and alteration of perlite and

807 rhyolite. J. Geol. Soc. London. 166, 895–904.

808 Drief, A., Schiffman, P., 2004. Very low-temperature alteration of sideromelane in hyaloclastites and
809 hyalotuffs from Kilauea and Mauna Kea volcanoes: implications for the mechanism of palagonite
810 formation. Clays Clay Miner. 52, 622–634.

811 Eggertsson, G.H., Kendrick, J.E., Weaver, J., Wallace, P.A., Utley, J.E.P., Bedford, J.D., Allen, M.J.,
812 Markússon, S.H., Worden, R.H., Faulkner, D.R., Lavallée, Y., n.d. Compaction of hyaloclastite from
813 the active geothermal system at Krafla volcano, Iceland, Submitted to this volume, Geofluids.

814 Eggertsson, G.H., Lavallée, Y., Kendrick, J.E., Markússon, S.H., 2018. Improving fluid flow in geothermal
815 reservoirs by thermal and mechanical stimulation: The case of Krafla volcano, Iceland. J.
816 Volcanol. Geotherm. Res.

817 Farquharson, J., Heap, M.J., Baud, P., Reuschlé, T., Varley, N.R., 2016. Pore pressure embrittlement in
818 a volcanic edifice. Bull. Volcanol. 78, 6.

819 Farquharson, J.I., Wadsworth, F.B., Heap, M.J., Baud, P., 2017. Time-dependent permeability evolution
820 in compacting volcanic fracture systems and implications for gas overpressure. J. Volcanol.
821 Geotherm. Res. 339, 81–97.

822 Ferrer, M., Seisdedos, J., de Vallejo, L.I., others, 2010. The role of hyaloclastite rocks in the stability of
823 the volcanic island flank of Tenerife. Volcan. Rock Mech. Taylor Fr. Group, London 167–170.

824 Forchheimer, P., 1901. Wasserbewegung durch boden. Z. Ver. Deutsch, Ing. 45, 1782–1788.

825 Franzson, H., Gu\dhfinnsson, G.H., Helgadóttir, H.M., Frolova, J., 2010. Porosity, density and chemical
826 composition relationships in altered Icelandic hyaloclastites. CRC Press Inc.

827 Fridleifsson, G., Ármannsson, H., Mortensen, A.K., 2006. Geothermal conditions in the Krafla caldera
828 with focus on well KG-26. Icel. Geosurvey Reykjavik, Icel.

829 Gautason, E., Blischke, A., Danielsen, P.E., 2007. Krafla: Borun tveggjakjarnaholna, KH-5 og KH-6
830 veturinn 2006–2007. ÍSOR technical report 07075,Reykjavik 22.

831 Ghassemi, A., Kumar, G.S., 2007. Changes in fracture aperture and fluid pressure due to thermal stress
832 and silica dissolution/precipitation induced by heat extraction from subsurface rocks.
833 Geothermics 36, 115–140.

834 Giordano, D., Russell, J.K., Dingwell, D.B., 2008. Viscosity of magmatic liquids: a model. Earth Planet.
835 Sci. Lett. 271, 123–134.

836 Gudmundsson, B.T., Arnórsson, S., 2002. Geochemical monitoring of the Krafla and Námafjall
837 geothermal areas, N-Iceland. Geothermics 31, 195–243.

838 Gysi, A.P., Stefánsson, A., 2012. Mineralogical aspects of CO2 sequestration during hydrothermal
839 basalt alteration—An experimental study at 75 to 250 C and elevated pCO2. Chem. Geol. 306,
840 146–159.

841 Harnett, C.E., Kendrick, J.E., Lamur, A., Thomas, M.E., Stinton, A., Wallace, P.A., Utley, J.E.P., Murphy,
842 W., Neuberg, J., Lavallée, Y., 2019. Evolution of Mechanical Properties of Lava Dome Rocks Across
843 the 1995--2010 Eruption of Soufrière Hills Volcano, Montserrat. Front. Earth Sci. 7.

844 Heap, M.J., Farquharson, J.I., Baud, P., Lavallée, Y., Reuschlé, T., 2015. Fracture and compaction of
845 andesite in a volcanic edifice. Bull. Volcanol. 77, 55.

846 Heap, M.J., Kennedy, B.M., 2016. Exploring the scale-dependent permeability of fractured andesite.
847 Earth Planet. Sci. Lett. 447, 139–150.

848 Heap, M.J., Lavallée, Y., Laumann, A., Hess, K.-U., Meredith, P.G., Dingwell, D.B., 2012. How tough is
849 tuff in the event of fire? Geology 40, 311–314.

850 Heap, M.J., Lavallée, Y., Laumann, A., Hess, K.-U., Meredith, P.G., Dingwell, D.B., Huismann, S., Weise,
851 F., 2013a. The influence of thermal-stressing (up to 1000 C) on the physical, mechanical, and
852 chemical properties of siliceous-aggregate, high-strength concrete. Constr. Build. Mater. 42,
853 248–265.

854 Heap, M.J., Lavallée, Y., Petrakova, L., Baud, P., Reuschle, T., Varley, N.R., Dingwell, D.B., 2014a.
855 Microstructural controls on the physical and mechanical properties of edifice-forming andesites
856 at Volcán de Colima, Mexico. J. Geophys. Res. Solid Earth 119, 2925–2963.

857 Heap, M.J., Mollo, S., Vinciguerra, S., Lavallée, Y., Hess, K.-U., Dingwell, D.B., Baud, P., Iezzi, G., 2013b.
858 Thermal weakening of the carbonate basement under Mt. Etna volcano (Italy): implications for
859 volcano instability. J. Volcanol. Geotherm. Res. 250, 42–60.

860 Heap, M.J., Xu, T., Chen, C., 2014b. The influence of porosity and vesicle size on the brittle strength of
861 volcanic rocks and magma. Bull. Volcanol. 76, 856.

862 Hekinian, R., Pineau, F., Shilobreeva, S., Bideau, D., Gracia, E., Javoy, M., 2000. Deep sea explosive
863 activity on the Mid-Atlantic Ridge near 34 50’ N: Magma composition, vesicularity and volatile
864 content. J. Volcanol. Geotherm. Res. 98, 49–77.

865 Honnorez, J., Kirst, P., 1975. Submarine basaltic volcanism: morphometric parameters for

discriminating hyaloclastites from hyalotuffs. Bull. Volcanol. 39, 441.

Hornby, A., Lavallée, Y., Kendrick, J.E., De Angelis, S., Lamur, A., Lamb, O.D., Rietbrock, A., Chigna, G., 2019. Brittle-ductile deformation and tensile rupture of dome lava during inflation at Santiaguito, Guatemala. J. Geophys. Res. Solid Earth.

Jakobsson, S.P., Gudmundsson, M.T., 2008. Subglacial and intraglacial volcanic formations in Iceland. Jökull 58, 179–196.

Jarosch, A., Gudmundsson, M.T., Högnadóttir, T., Axelsson, G., 2008. Progressive cooling of the hyaloclastite ridge at Gjálp, Iceland, 1996--2005. J. Volcanol. Geotherm. Res. 170, 218–229.

Kawano, M., Tomita, K., 1991. Dehydration and rehydration of saponite and vermiculite. Clays Clay Miner. 39, 174–183.

Kendrick, J.E., Smith, R., Sammonds, P., Meredith, P.G., Dainty, M., Pallister, J.S., 2013. The influence of thermal and cyclic stressing on the strength of rocks from Mount St. Helens, Washington. Bull. Volcanol. 75, 728.

Kim, K.-Y., Park, Y.-S., Kim, G.-P., Park, K.-H., 2009. Dynamic freshwater--saline water interaction in the coastal zone of Jeju Island, South Korea. Hydrogeol. J. 17, 617–629.

Klinkenberg, L.J., 1941. The permeability of porous media to liquids and gases, in: Drilling and Production Practice.

Kokelaar, P., 1986. Magma-water interactions in subaqueous and emergent basaltic. Bull. Volcanol. 48, 275–289.

Kolaříková, I., Přikryl, R., Hanus, R., Jelínek, E., 2005. Thermal loading of smectite-rich rocks: natural processes vs. laboratory experiments. Appl. Clay Sci. 29, 215–223.

Kristmannsdóttir, H., 1979. Alteration of Basaltic Rocks by Hydrothermal-Activity at 100-300 C, in: Developments in Sedimentology. Elsevier, pp. 359–367.

Kumar, G.S., Ghassemi, A., 2005. Numerical modeling of non-isothermal quartz dissolution/precipitation in a coupled fracture--matrix system. Geothermics 34, 411–439.

Kwon, O., Herbert, B.E., Kronenberg, A.K., 2004. Permeability of illite-bearing shale: 2. Influence of fluid chemistry on flow and functionally connected pores. J. Geophys. Res. Solid Earth 109.

Lamur, A., Kendrick, J.E., Eggertsson, G.H., Wall, R.J., Ashworth, J.D., Lavallée, Y., 2017. The permeability of fractured rocks in pressurised volcanic and geothermal systems. Sci. Rep. 7, 1–9.

Lévy, L., Gibert, B., Sigmundsson, F., Flóvenz, Ó.G., Hersir, G.P., Briole, P., Pezard, P.A., 2018. The role of smectites in the electrical conductivity of active hydrothermal systems: electrical properties of core samples from Krafla volcano, Iceland. Geophys. J. Int. 215, 1558–1582.

Malek, Z., Balek, V., Garfinkel-Shweky, D., Yariv, S., 1997. The study of the dehydration and dehydroxylation of smectites by emanation thermal analysis. J. Therm. Anal. 48, 83–92.

Marks, N., Schiffman, P., Zierenberg, R.A., Franzson, H., Fridleifsson, G.Ó., 2010. Hydrothermal alteration in the Reykjanes geothermal system: Insights from Iceland deep drilling program well RN-17. J. Volcanol. Geotherm. Res. 189, 172–190.

Matter, J.M., Broecker, W.S., Gislason, S.R., Gunnlaugsson, E., Oelkers, E.H., Stute, M., Sigurdardóttir, H., Stefansson, A., Alfre\dhsson, H.A., Aradóttir, E.S., others, 2011. The CarbFix Pilot Project--storing carbon dioxide in basalt. Energy Procedia 4, 5579–5585.

Mayer, K., Scheu, B., Gilg, H.A., Heap, M.J., Kennedy, B.M., Lavallée, Y., Letham-Brake, M., Dingwell, D.B., 2015. Experimental constraints on phreatic eruption processes at Whakaari (White Island volcano). J. Volcanol. Geotherm. Res. 302, 150–162.

Milliken, R.E., Mustard, J.F., 2005. Quantifying absolute water content of minerals using near-infrared reflectance spectroscopy. J. Geophys. Res. Planets 110.

Mitchell, N.C., 2003. Susceptibility of mid-ocean ridge volcanic islands and seamounts to large-scale landsliding. J. Geophys. Res. Solid Earth 108.

Mordensky, S.P., Kennedy, B.M., Villeneuve, M.C., Lavallée, Y., Reichow, M.K., Wallace, P.A., Siratovich, P.A., Gravley, D.M., 2019. Increasing the permeability of hydrothermally altered andesite by transitory heating. Geochemistry, Geophys. Geosystems.

Mortensen, A.K., Egilson, \TH, Gautason, B., Árnadóttir, S., Gu\dhmundsson, Á., 2014. Stratigraphy, alteration mineralogy, permeability and temperature conditions of well IDDP-1, Krafla, NE-Iceland. Geothermics 49, 31–41.

Mosser-Ruck, R., Devineau, K., Charpentier, D., Cathelineau, M., 2005. Effects of ethylene glycol saturation protocols on XRD patterns: a critical review and discussion. Clays Clay Miner. 53, 631–638.

Nielson, D.L., Stiger, S.G., 1996. Drilling and evaluation of Ascension# 1, a geothermal exploration well on Ascension Island, South Atlantic Ocean. Geothermics 25, 543–560.

Oelkers, E.H., Gislason, S.R., 2001. The mechanism, rates and consequences of basaltic glass

925 dissolution: I. An experimental study of the dissolution rates of basaltic glass as a function of
926 aqueous Al, Si and oxalic acid concentration at 25 C and pH= 3 and 11. Geochim. Cosmochim.
927 Acta 65, 3671–3681.

928 Richter, D., Simmons, G., 1974. Thermal expansion behavior of igneous rocks, in: International Journal
929 of Rock Mechanics and Mining Sciences & Geomechanics Abstracts. pp. 403–411.

930 Robert, G., Whittington, A.G., Stechern, A., Behrens, H., 2014. Heat capacity of hydrous basaltic glasses
931 and liquids. J. Non. Cryst. Solids 390, 19–30.

932 Russell, J.D. t, Farmer, V.C., 1964. Infra-red spectroscopic study of the dehydration of montmorillonite
933 and saponite. Clay Miner. Bull. 5, 443–464.

934 Sammis, C.G., Ashby, M.F., 1986. The failure of brittle porous solids under compressive stress states.
935 Acta Metall. 34, 511–526.

936 Schaefer, L.N., Kendrick, J.E., Oommen, T., Lavallée, Y., Chigna, G., 2015. Geomechanical rock
937 properties of a basaltic volcano. Front. Earth Sci. 3, 29.

938 Schauroth, J., Wadsworth, F.B., Kennedy, B., von Aulock, F.W., Lavallée, Y., Damby, D.E., Vasseur, J.,
939 Scheu, B., Dingwell, D.B., 2016. Conduit margin heating and deformation during the AD 1886
940 basaltic Plinian eruption at Tarawera volcano, New Zealand. Bull. Volcanol. 78, 12.

941 Schiffman, P., Watters, R.J., Thompson, N., Walton, A.W., 2006. Hyaloclastites and the slope stability
942 of Hawaiian volcanoes: Insights from the Hawaiian Scientific Drilling Project's 3-km drill core. J.
943 Volcanol. Geotherm. Res. 151, 217–228.

944 Schopka, H.H., Gudmundsson, M.T., Tuffen, H., 2006. The formation of Helgafell, southwest Iceland, a
945 monogenetic subglacial hyaloclastite ridge: sedimentology, hydrology and volcano--ice
946 interaction. J. Volcanol. Geotherm. Res. 152, 359–377.

947 Scott, S.W., Covell, C., Júl\'\iusson, E., Valfells, Á., Newson, J., Hrafnkelsson, B., Pálsson, H.,
948 Gudjónsdóttir, M., 2019. A probabilistic geologic model of the Krafla geothermal system
949 constrained by gravimetric data. Geotherm. Energy 7, 1–30.

950 Segall, P., Fitzgerald, S.D., 1998. A note on induced stress changes in hydrocarbon and geothermal
951 reservoirs. Tectonophysics 289, 117–128.

952 Senger, K., Tveranger, J., Planke, S., Ogata, K., Braathen, A., Wheeler, W., Chevallier, L., 2012. Fluid
953 flow around igneous intrusions: from outcrop to simulator, in: LASI 5 Conference, 29--30
954 October, Port Elizabeth, South Africa. pp. 2–3.

955 Shirozu, H., Sakasegawa, T., Katsumoto, N., Ozaki, M., 1975. Mg-chlorite and interstratified Mg-
956 chlorite/saponite associated with Kuroko deposits. Clay Sci. 4, 305–321.
957 https://doi.org/10.11362/jcssjclayscience1960.4.305

958 Siratovich, P.A., Heap, M.J., Villenueve, M.C., Cole, J.W., Reuschlé, T., 2014. Physical property
959 relationships of the Rotokawa Andesite, a significant geothermal reservoir rock in the Taupo
960 Volcanic Zone, New Zealand. Geotherm. Energy 2, 10.

961 Siratovich, P.A., Sass, I., Homuth, S., Bjornsson, A., 2011. Thermal stimulation of geothermal reservoirs
962 and laboratory investigation of thermally-induced fractures, in: Proc., Geothermal Resources
963 Council Annual Meeting. pp. 1529–1535.

964 Siratovich, P.A., Villeneuve, M.C., Cole, J.W., Kennedy, B.M., Bégué, F., 2015. Saturated heating and
965 quenching of three crustal rocks and implications for thermal stimulation of permeability in
966 geothermal reservoirs. Int. J. Rock Mech. Min. Sci. 80, 265–280.

967 Stroncik, N.A., Schmincke, H.-U., 2001. Evolution of palagonite: Crystallization, chemical changes, and
968 element budget. Geochemistry, Geophys. Geosystems 2.

969 Tuffen, H., Castro, J.M., 2009. The emplacement of an obsidian dyke through thin ice:
970 Hrafntinnuhryggur, Krafla Iceland. J. Volcanol. Geotherm. Res. 185, 352–366.

971 Tulinius, H., Correia, H., Sigurdsson, O., 2000. Stimulating a high enthalpy well by thermal cracking, in:
972 World Geothermal Congress.

973 Van Otterloo, J., Cas, R.A.F., Scutter, C.R., 2015. The fracture behaviour of volcanic glass and relevance
974 to quench fragmentation during formation of hyaloclastite and phreatomagmatism. Earth-
975 Science Rev. 151, 79–116.

976 Vasseur, J., Wadsworth, F.B., Lavallée, Y., Hess, K.-U., Dingwell, D.B., 2013. Volcanic sintering:
977 timescales of viscous densification and strength recovery. Geophys. Res. Lett. 40, 5658–5664.

978 Vidal, O., Dubacq, B., 2009. Thermodynamic modelling of clay dehydration, stability and compositional
979 evolution with temperature, pressure and H2O activity. Geochim. Cosmochim. Acta 73, 6544–
980 6564.

981 von Aulock, F.W., Nichols, A.R.L., Kennedy, B.M., Oze, C., 2013. Timescales of texture development in
982 a cooling lava dome. Geochim. Cosmochim. Acta 114, 72–80.

983 Wang, W.-H., Wong, T., 2003. Effects of reaction kinetics and fluid drainage on the development of
984 pore pressure excess in a dehydrating system. Tectonophysics 370, 227–239.

985 Wohletz, K.H., 1986. Explosive magma-water interactions: Thermodynamics, explosion mechanisms,
986 and field studies. Bull. Volcanol. 48, 245–264.

987 Wohletz, K.H., Sheridan, M.F., 1983. Hydrovolcanic explosions; II, Evolution of basaltic tuff rings and
988 tuff cones. Am. J. Sci. 283, 385–413.

989 Wright, J. V, Cas, R.A.F., 1988. Volcanic successions, modern and ancient: a geological approach to
990 processes, products, and successions. London; Boston: Allen & Unwin/Chapman & Hall.

991 Yariv, S., Ovadyahu, D., Nasser, A., Shuali, U., Lahav, N., 1992. Thermal analysis study of heat of
992 dehydration of tributylammonium smectites. Thermochim. Acta 207, 103–113.

993 Yen, A.S., Murray, B.C., Rossman, G.R., 1998. Water content of the Martian soil: Laboratory
994 simulations of reflectance spectra. J. Geophys. Res. Planets 103, 11125–11133.

995 Yong, C., Wang, C., 1980. Thermally induced acoustic emission in Westerly granite. Geophys. Res. Lett.
996 7, 1089–1092.

997 Zakharova, O.K., Spichak, V. V, 2012. Geothermal fields of Hengill Volcano, Iceland. J. Volcanol.
998 Seismol. 6, 1–14.

999 Zhang, J., Wong, T.-F., Davis, D.M., 1990. Micromechanics of pressure-induced grain crushing in porous
1000 rocks. J. Geophys. Res. Solid Earth 95, 341–352.

1001 Zhang, Y., 1999. A criterion for the fragmentation of bubbly magma based on brittle failure theory.
1002 Nature 402, 648.

1003 Zhu, W., Baud, P., Wong, T., 2010. Micromechanics of cataclastic pore collapse in limestone. J.
1004 Geophys. Res. Solid Earth 115.

1005

Supplementary information for "**Thermal liability of hyaloclastite in the Krafla geothermal reservoir, Iceland: the impact of phyllosilicates on permeability and rock strength"**

Josh Weaver[1*], Guðjón H. Eggertsson[1], James E.P. Utley[1], Paul A. Wallace[1], Anthony Lamur[1], Jackie E. Kendrick[1], Hugh Tuffen[2], Sigurður H. Markússon[3], Yan Lavallée[1].

[1]Department of Earth, Ocean and Ecological Sciences, University of Liverpool, 4 Brownlow Street, L69 3GP, Liverpool, UK

[2]Lancaster Environment Centre, Lancaster University, LA1 4YQ, Lancaster, UK

[3]Landsvirkjun, Háaleitisbraut 68, 110 Reykjavík, Iceland

*j.weaver@liverpool.ac.uk

This file contains the supplementary information used for analysis in the main paper.

1. Sample Physical and Mechanical Data

Table S1. A summary of water permeability values at a range of confining pressures.

Sample	Confining pressure	K	Porosity reduction
	(MPa)	(m^2)	(%)
HYA_0m_002	3.73	8.05E-14	n/a
	7.95	7.51E-14	0
	12.53	6.46E-14	0.49
	16.96	4.87E-14	0.89
	23.75	2.18E-15	2.31
	28.8	1.13E-15	3.25
HYA_0m_006	3.55	4.68E-14	n/a
	9.04	5.58E-14	0
	13.96	7.18E-14	0.66
	18.91	4.96E-14	1.49
	23.84	2.25E-14	2.53
	29.04	8.13E-15	3.84
HYA_0m_008	3.94	7.87E-14	n/a
	8.78	7.15E-14	0
	13.83	6.28E-14	0.94
	18.78	5.07E-14	1.92
	23.67	3.65E-14	3
	27.9	2.14E-14	4.05
HYA_0m_015	3.55	1.56E-14	n/a
	8.65	1.85E-14	0

	13.6	1.68E-14	0.34
	18.65	1.63E-14	0.91
	23.7	1.26E-14	1.92
	28.65	4.37E-15	3.47
	33.26	5.34E-16	5.21
HYA_0m_020	3.58	5.48E-16	n/a
	8.53	4.42E-16	0
	13.61	3.98E-16	0.41
	18.51	7.72E-16	1
	23.56	2.67E-16	1.93
	28.21	8.93E-16	3.22
HYA_0m_021	3.89	1.63E-14	n/a
	8.84	1.61E-14	0
	13.54	1.56E-14	0.75
	18.5	1.47E-14	1.64
	23.46	1.24E-14	2.91
	28.4	3.59E-15	4.53
HYA_0m_035	3.27	2.28E-15	n/a
	8.85	5.20E-15	0
	13.89	6.06E-15	1.3
	19.28	6.58E-15	2.54
	23.97	7.01E-15	3.53
	28.36	6.00E-15	4.36
HYA_0m_068	3.71	5.77E-15	n/a
	8.58	4.66E-15	0
	13.78	1.28E-14	1.25
	18.75	1.78E-14	2.29
	23.45	1.53E-14	2.52
	28.59	1.31E-14	3.49
HYA_0m_072	3.78	2.24E-13	n/a
	8.89	1.59E-13	0
	13.7	1.37E-13	1.32
	18.98	1.08E-13	2.55
	23.7	1.04E-13	3.78
	28.79	8.21E-14	4.8
HYA_0m_076	3.46	1.10E-13	n/a
	8.82	8.96E-14	0
	13.78	8.01E-14	1.24
	18.35	6.93E-14	2.38
	23.47	5.82E-14	3.67
	28.51	4.78E-14	4.5

16 Table S2. A summary of all porosity, gas permeability, compressive strength and Young's Modulus values for as-collected and thermally treated cores.

As-collected					Post-thermal treatment						
Sample	Density	Porosity	Gas K	TT	Density	Mass reduction	Porosity	Gas K	UCS	TXL	Young's Modulus
	(g/cm^3)	(%)	(m^2)	(°C)	(g/cm^3)	(g)	(%)	(m^2)	(MPa)	(MPa)	(GPa)
HYA_0m_001	2.5084	37.17	1.81E-13	n/a	n/a	n/a	n/a	n/a	n/a	n/a	n/a
HYA_0m_002	2.5016	37.58	1.33E-13	130	2.5876	1.94	40.7	1.65E-13	n/a	n/a	n/a
HYA_0m_003	2.5383	39.99	2.95E-13	130	2.6197	1.51	42.1	3.66E-13	n/a	n/a	n/a
HYA_0m_004	2.5397	38.4	2.18E-13	130	2.628	1.65	41.5	2.66E-13	n/a	n/a	n/a
HYA_0m_005	2.5405	38.24	2.89E-13	130	2.6247	1.5	42.4	3.63E-13	n/a	n/a	n/a
HYA_0m_006	2.5527	36.75	1.53E-13	185	2.6204	1.02	42.2	2.30E-13	n/a	n/a	n/a
HYA_0m_007	2.5015	34.38	7.21E-14	185	2.6145	2.06	40.2	1.24E-13	n/a	n/a	n/a
HYA_0m_008	2.506	36.08	1.34E-13	185	2.6222	1.95	41.8	2.23E-13	n/a	n/a	n/a
HYA_0m_009	2.5515	39.06	1.87E-13	185	2.6173	0.94	42	2.47E-13	n/a	n/a	n/a
HYA_0m_010	2.5691	40.29	2.72E-13	n/a	n/a	n/a	n/a	n/a	n/a	n/a	n/a
HYA_0m_011	2.5496	38.48	2.76E-13	n/a	n/a	n/a	n/a	n/a	n/a	n/a	n/a
HYA_0m_012	2.5719	40.93	3.20E-13	130	2.6214	0.76	43.1	3.71E-13	8.8	n/a	1.58
HYA_0m_013	2.5219	38.7	2.14E-13	n/a	n/a	n/a	n/a	n/a	n/a	n/a	n/a
HYA_0m_014	2.5396	36.75	2.45E-13	n/a	n/a	n/a	n/a	n/a	n/a	n/a	n/a
HYA_0m_015	2.4945	36.76	1.50E-13	n/a	n/a	n/a	n/a	n/a	n/a	n/a	n/a
HYA_0m_016	2.5639	37.69	3.69E-13	n/a	n/a	n/a	n/a	n/a	n/a	n/a	n/a
HYA_0m_017	2.5818	38.33	4.12E-13	n/a	n/a	n/a	n/a	n/a	n/a	n/a	n/a
HYA_0m_018	2.5358	38.24	2.61E-13	185	2.6452	1.71	43.3	3.68E-13	n/a	n/a	n/a
HYA_0m_019	2.5099	37.62	1.31E-13	185	2.6298	2.04	43.5	2.14E-13	n/a	n/a	n/a
HYA_0m_020	2.5017	36.65	1.47E-13	n/a	n/a	n/a	n/a	n/a	n/a	n/a	n/a

HYA_0m_021	2.5153	37.65	1.85E-13	130	2.6033	1.62	42.1	2.48E-13	n/a	n/a	n/a
HYA_0m_022	2.5067	38.29	1.86E-13	n/a	n/a	n/a	n/a	n/a	n/a	n/a	n/a
HYA_0m_023	2.5323	36.14	1.81E-13	185	2.6433	1.88	41.5	2.77E-13	n/a	n/a	n/a
HYA_0m_024	2.5975	41.82	3.72E-13	n/a	n/a	n/a	n/a	n/a	8	n/a	1.15
HYA_0m_025	2.5596	39.86	2.42E-13	185	2.6195	0.79	42.4	3.02E-13	92	n/a	0.95
HYA_0m_026	2.5767	39.67	2.21E-13	130	2.612	0.51	41.2	2.54E-13	11.5	n/a	1.91
HYA_0m_027	2.5568	40.45	1.91E-13	130	2.5925	0.45	42.1	2.21E-13	8.7	n/a	1
HYA_0m_028	2.5686	41.75	2.41E-13	185	2.6314	0.74	44.2	3.07E-13	6.3	n/a	0.66
HYA_0m_029	2.5631	39.98	1.98E-13	n/a	n/a	n/a	n/a	n/a	10.1	n/a	1.43
HYA_0m_030	2.5592	41.31	2.03E-13	n/a	n/a	n/a	n/a	n/a	8.3	n/a	1.18
HYA_0m_031	2.5531	39.84	1.75E-13	130	2.5938	0.54	41.6	2.03E-13	8.4	n/a	1.3
HYA_0m_032	2.5471	40.24	1.30E-13	185	2.6178	0.86	43.1	1.74E-13	10.5	n/a	1.41
HYA_0m_033	2.6043	40.8	4.13E-13	185	2.6558	0.7	43	4.90E-13	7	n/a	0.85
HYA_0m_034	2.5514	44.13	2.50E-13	600	2.7653	2.77	45.9	5.90E-13	6.6	n/a	0.73
HYA_0m_035	2.5036	37.96	1.70E-13	600	2.7355	3.58	47.9	5.46E-13	n/a	n/a	n/a
HYA_0m_036	2.5119	41.36	1.79E-13	600	2.7273	3.02	50.3	5.56E-13	4.2	n/a	0.49
HYA_0m_037	2.5027	37.66	2.08E-13	600	2.7279	2.74	47.1	5.55E-13	n/a	n/a	n/a
HYA_0m_038	2.527	37.89	2.17E-13	600	2.7489	2.92	47	5.68E-13	n/a	n/a	n/a
HYA_0m_039	2.5107	39.42	1.94E-13	600	2.7325	3.21	48.7	5.86E-13	5.3	n/a	0.47
HYA_0m_040	2.4976	35.7	1.73E-13	130	2.5302	0.38	39	2.13E-13	n/a	n/a	n/a
HYA_0m_041	2.5636	37.66	3.60E-13	600	2.7633	2.64	46	7.04E-13	n/a	23.1	0.56
HYA_0m_042	2.5348	40.85	2.12E-13	185	2.6498	0.61	44.3	n/a	n/a	23.8	1.79
HYA_0m_043	2.5488	40.33	2.23E-13	185	2.62	1.16	43.7	n/a	n/a	26.3	1.38
HYA_0m_044	2.5556	40.23	2.29E-13	130	2.5878	0.42	41.6	n/a	n/a	27.7	2.51
HYA_0m_045	2.5548	40.76	2.51E-13	n/a	n/a	n/a	n/a	n/a	n/a	n/a	n/a
HYA_0m_046	2.5687	40.59	2.81E-13	n/a	n/a	n/a	n/a	n/a	n/a	n/a	n/a
HYA_0m_047	2.5582	39.91	2.60E-13	n/a	n/a	n/a	n/a	n/a	n/a	29.5	3.44
HYA_0m_048	2.5523	40.37	2.08E-13	n/a	n/a	n/a	n/a	n/a	n/a	n/a	n/a

HYA_0m_049	2.5345	38.59	1.44E-13	n/a	n/a	n/a	n/a	n/a	n/a	n/a	n/a
HYA_0m_050	2.5426	39.04	2.39E-13	n/a	n/a	n/a	n/a	n/a	n/a	n/a	n/a
HYA_0m_051	2.5562	39.35	1.69E-13	n/a	n/a	n/a	n/a	n/a	n/a	n/a	n/a
HYA_0m_052	2.532	39.92	1.47E-13	n/a	n/a	n/a	n/a	n/a	n/a	n/a	n/a
HYA_0m_053	2.5858	40.02	3.35E-13	400	2.7271	1.9	45.8	5.47E-13	n/a	n/a	n/a
HYA_0m_054	2.5386	38.23	2.11E-13	400	2.6862	1.99	44.2	3.61E-13	n/a	26.3	1.33
HYA_0m_055	2.6033	40.35	4.80E-13	400	2.7385	1.84	45.8	7.53E-13	n/a	n/a	n/a
HYA_0m_056	2.5337	39.83	1.86E-13	600	2.7103	2.3	47	4.50E-13	n/a	24.1	0.68
HYA_0m_057	2.5467	40.02	2.39E-13	400	2.6791	1.84	45.7	4.27E-13	6.8	n/a	1.27
HYA_0m_058	2.5504	39.76	2.54E-13	400	2.685	1.79	45.5	4.33E-13	n/a	n/a	n/a
HYA_0m_059	2.5885	38.33	3.54E-13	400	2.7295	1.82	44.2	5.69E-13	6.3	n/a	1.32
HYA_0m_060	2.543	41.08	2.11E-13	400	2.6927	1.85	47.1	4.01E-13	n/a	n/a	n/a
HYA_0m_061	2.5482	40.6	2.14E-13	400	2.6909	1.91	46.6	4.13E-13	n/a	n/a	n/a
HYA_0m_062	2.4618	36.8	n/a	n/a	n/a	n/a	n/a	n/a	n/a	n/a	n/a
HYA_0m_063	2.4676	37.79	n/a	n/a	n/a	n/a	n/a	n/a	n/a	n/a	n/a
HYA_0m_064	2.4674	36.81	n/a	n/a	n/a	n/a	n/a	n/a	n/a	n/a	n/a
HYA_0m_065	2.5072	39.93	n/a	n/a	n/a	n/a	n/a	n/a	n/a	n/a	n/a
HYA_0m_066	2.5087	36.96	n/a	n/a	n/a	n/a	n/a	n/a	n/a	n/a	n/a
HYA_0m_067	2.5482	39.29	1.82E-13	400	2.6286	0.9	42.5	3.10E-13	n/a	n/a	n/a
HYA_0m_068	2.5449	38.61	1.56E-13	400	2.6479	1.1	42.6	2.90E-13	n/a	n/a	n/a
HYA_0m_069	2.5515	39.27	1.82E-13	n/a	n/a	n/a	n/a	n/a	n/a	n/a	n/a
HYA_0m_070	2.5497	38.46	2.51E-13	n/a	n/a	n/a	n/a	n/a	n/a	31	2.17
HYA_0m_071	2.5376	39.01	1.97E-13	130	2.5678	0.61	40.6	2.29E-13	n/a	29.6	1.52
HYA_0m_072	2.5956	38.86	3.96E-13	600	2.7501	1.91	45.1	7.42E-13	n/a	n/a	n/a
HYA_0m_073	2.5492	40	2.12E-13	400	2.6811	1.89	45.6	3.82E-13	n/a	24.7	1.1
HYA_0m_074	2.5405	38.77	3.45E-13	n/a	n/a	n/a	n/a	n/a	n/a	n/a	n/a
HYA_0m_075	2.536	40.02	2.11E-13	400	2.6878	2.32	46.5	4.18E-13	5.9	n/a	0.8
HYA_0m_076	2.5992	38.34	4.27E-13	400	2.6612	1.04	41.3	6.46E-13	n/a	n/a	n/a

Table S3. A summary of the Brazilian disc parameters for as-collected and TT samples.

As-collected				Post-thermal treatment			
Sample	Density	Porosity	TT	Density	Mass Reduction	Porosity	UTS
	(g/cm^3)	(%)	(°C)	(g/cm^3)	(g)	(%)	(MPa)
HYA_0m_001_Br	2.4899	31.09	n/a	n/a	n/a	n/a	1.53
HYA_0m_002_Br	2.5139	33.67	n/a	n/a	n/a	n/a	1.21
HYA_0m_003_Br	2.4877	32.05	n/a	n/a	n/a	n/a	1.69
HYA_0m_004_Br	2.545	33.04	n/a	n/a	n/a	n/a	1.5
HYA_0m_005_Br	2.5824	32.28	130	2.6346	0.32	35.67	0.98
HYA_0m_006_Br	2.5626	36.44	130	2.6214	0.39	39.95	0.96
HYA_0m_007_Br	2.562	38.9	130	2.6166	0.42	42.4	0.92
HYA_0m_008_Br	2.5598	34.78	130	2.6157	0.36	38.41	1.07
HYA_0m_009_Br	2.5453	38.07	130	2.6059	0.39	41.69	0.79
HYA_0m_010_Br	2.5122	37.56	185	2.5993	0.47	42.36	0.97
HYA_0m_011_Br	2.6096	36.32	185	2.6402	0.33	38.99	0.82
HYA_0m_012_Br	2.52	41.33	185	2.6095	0.42	45.86	0.86
HYA_0m_013_Br	2.524	39.53	185	2.6098	0.49	43.86	0.91
HYA_0m_014_Br	2.4942	36.79	185	2.5956	0.59	42.22	1
HYA_0m_015_Br	2.5498	36.18	400	2.7235	0.76	44.47	0.7
HYA_0m_016_Br	2.568	39.51	400	2.6707	0.66	45.59	0.63
HYA_0m_017_Br	2.5964	35.17	400	2.707	0.66	41.5	0.68
HYA_0m_018_Br	2.518	40.18	400	2.6618	0.75	47.3	0.69
HYA_0m_019_Br	2.5002	36.55	400	2.6419	0.82	44.19	0.8
HYA_0m_020_Br	2.5171	39.02	600	2.6952	0.73	46.69	0.7
HYA_0m_021_Br	2.5885	35.91	600	2.776	0.79	40.97	0.66
HYA_0m_022_Br	2.5028	38.59	600	2.7167	0.98	48.32	0.57
HYA_0m_023_Br	2.5168	38.59	600	2.717	1.01	47.64	0.66
HYA_0m_024_Br	2.5295	35.99	600	2.7473	0.94	46.16	0.54

2. Clay-separated XRD

Clay separated XRD measurements were performed on as-collected, surficial hyaloclastite for unglycolated and glycolated samples. The d(060) peak is at 60.35°, whilst the d(001) peak transitions from 15 Å to 16.2 Å, upon glycolation. Raw X-ray diffractograms are presented in Figure SI1 a and b.

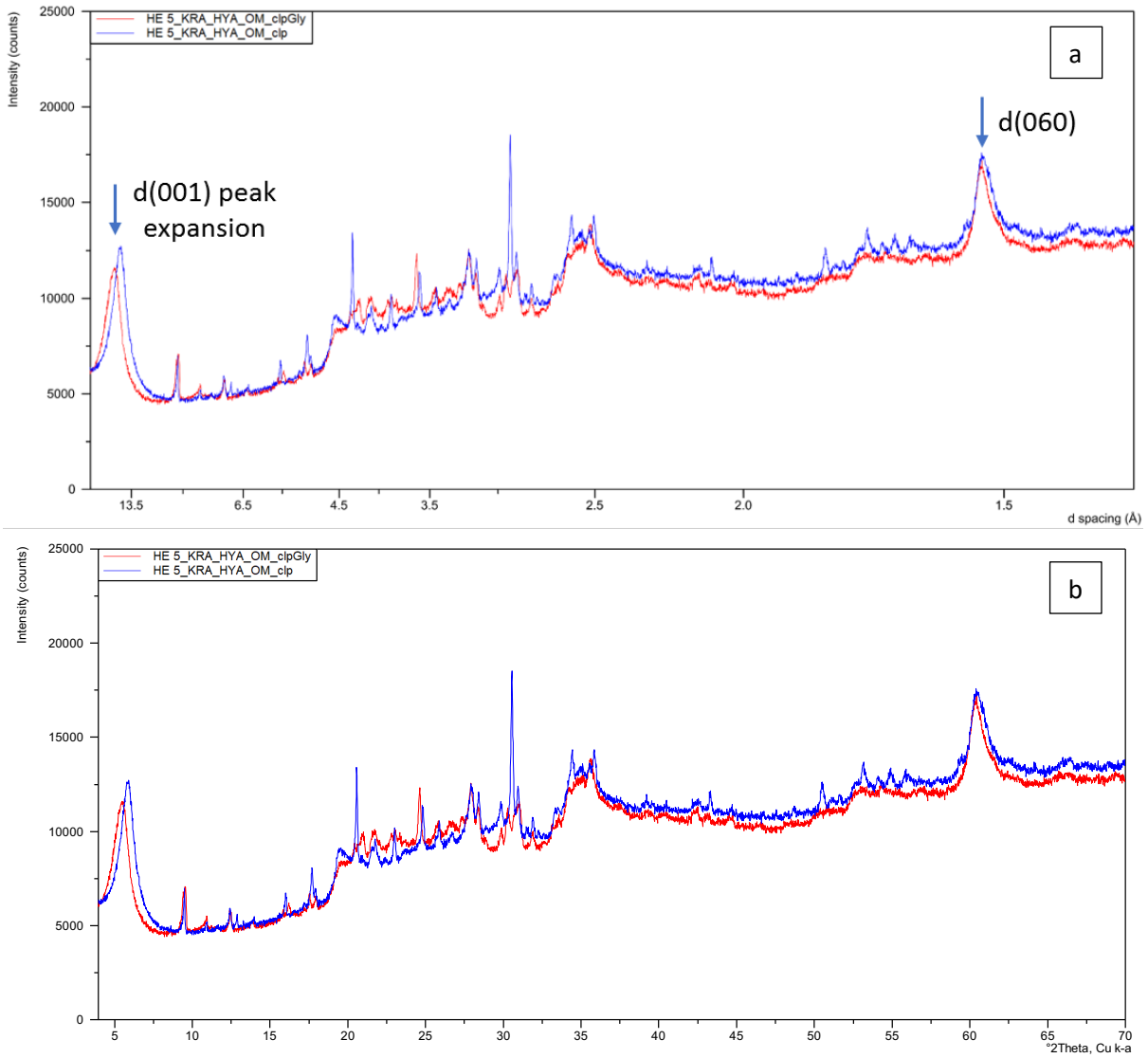

Figure S1. X-ray diffractograms of as-collected, gylcolated and unglycolated surficial hyaloclastite; **a.** intensity presented against °2Theta Cu k-a; **b**. intensity presented against angstroms.

3. QEMSCAN Images

We present here the full QEMSCAN images, acquired at 20 µm for as-collected (Fig. S2) and thermally treated (TT) samples (Fig. S3 – S6), that are used in the quantification of the mineral distribution (Table 2, main paper). Fig. S7 provides an annotated example of the various petrographic images presented in Figure 3 (main paper).

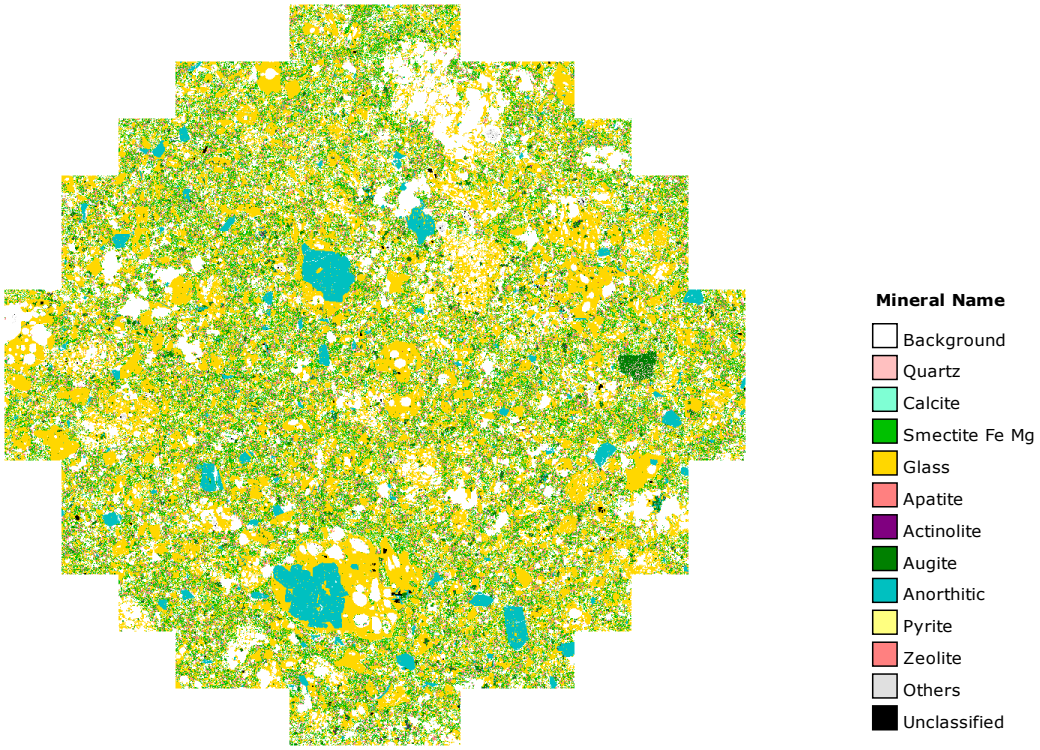

Figure S2. Mineral distribution of as-collected hyaloclastite, acquired using QEMSCAN at 20 µm resolution.

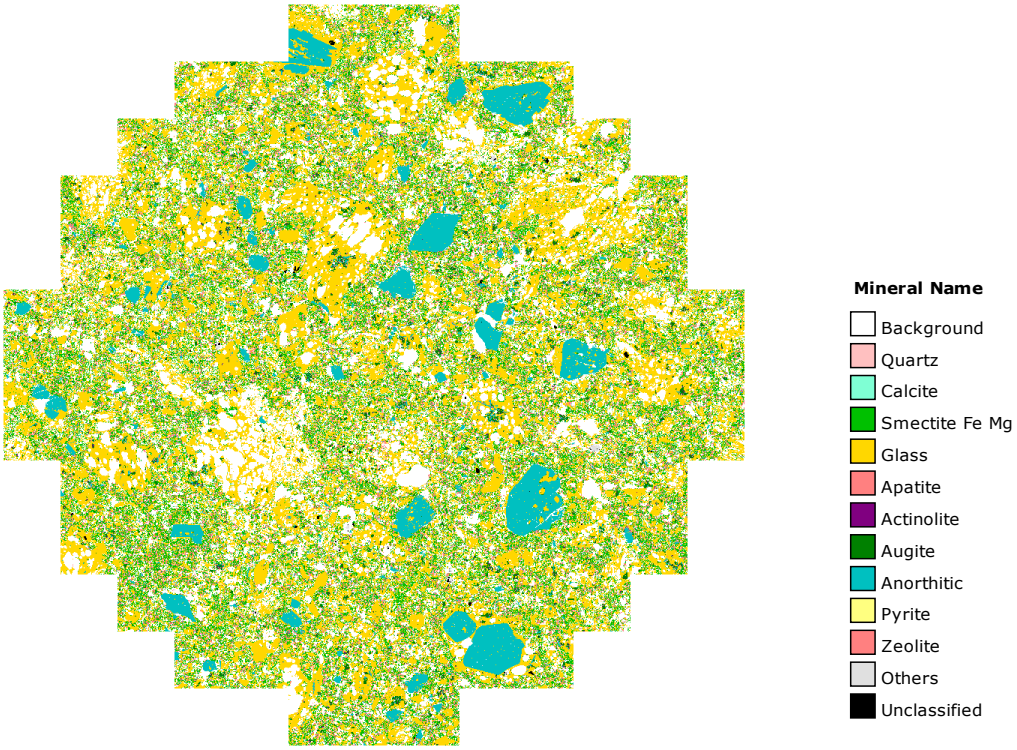

Figure S3. Mineral distribution of hyaloclastite, TT to 130 °C for 12 hours, and acquired using QEMSCAN at 20 µm resolution.

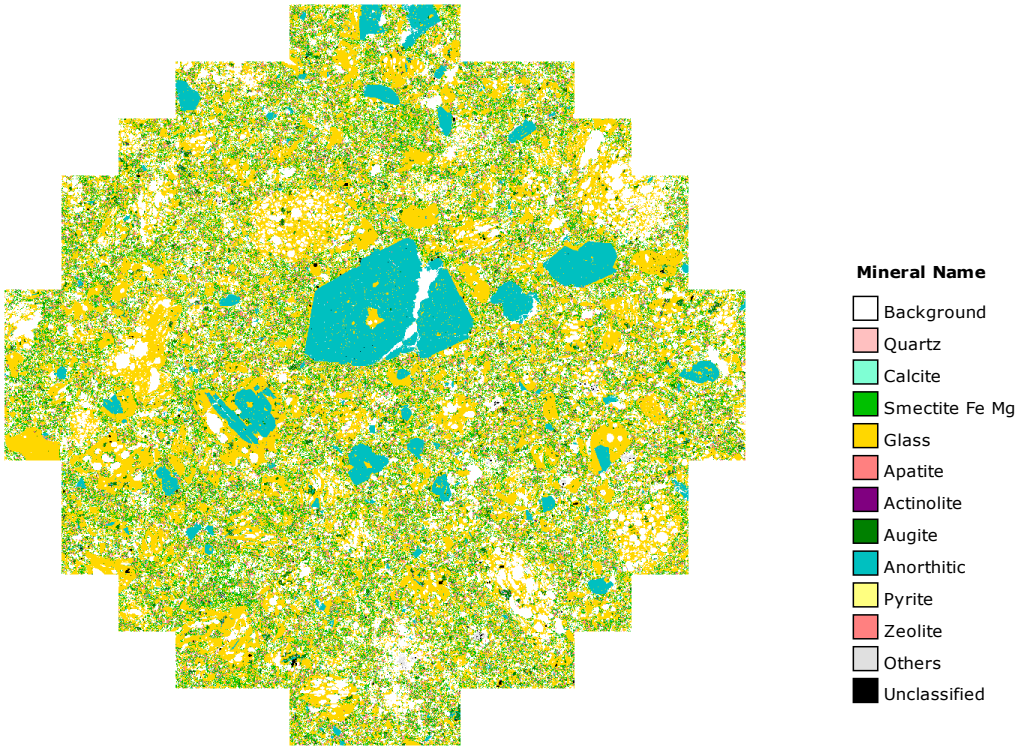

Figure S4. Mineral distribution of hyaloclastite, TT to 185 °C for 12 hours, and acquired using QEMSCAN at 20 µm resolution.

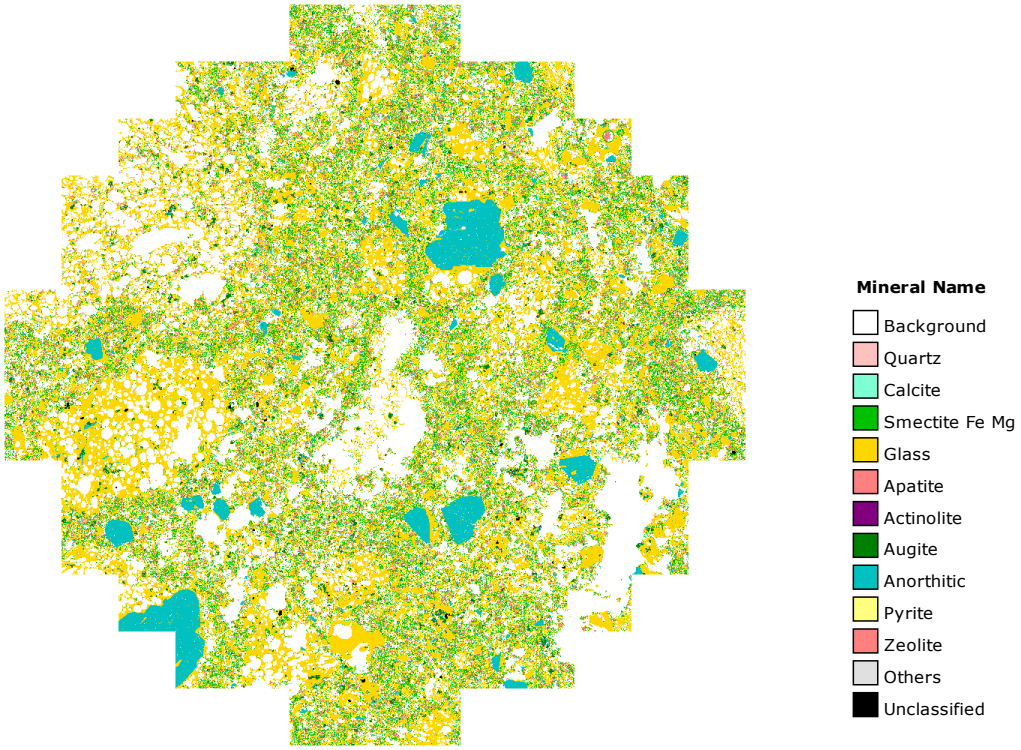

Figure S5. Mineral distribution of hyaloclastite, TT to 400 °C for 12 hours, and acquired using QEMSCAN at 20 µm resolution.

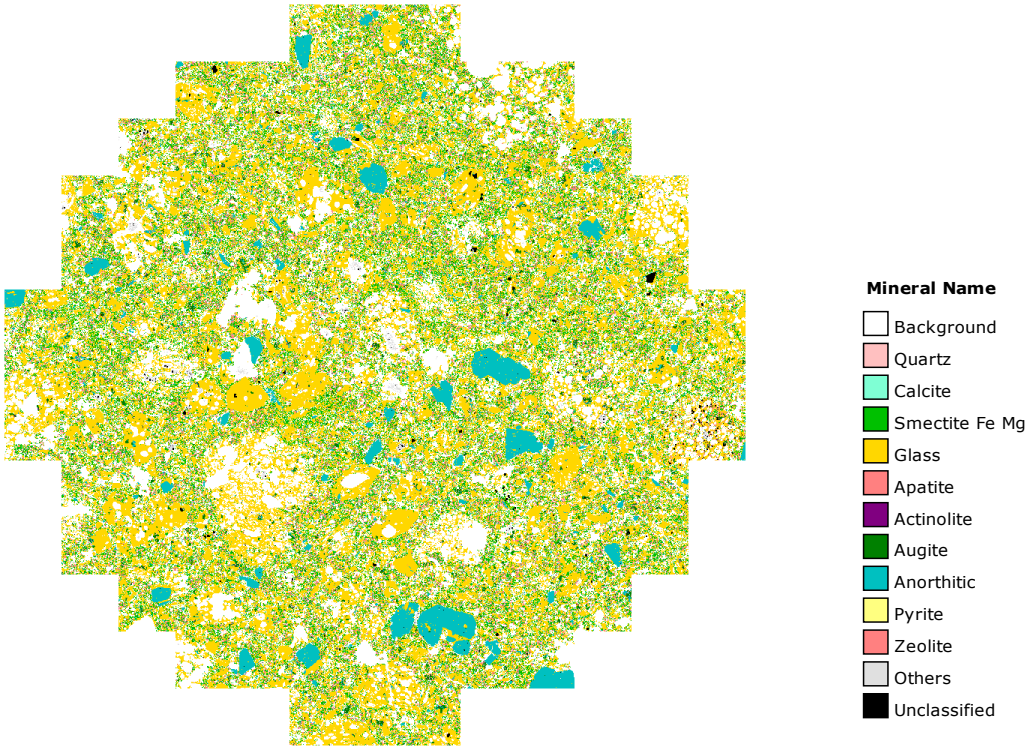

Figure S6. Mineral distribution of hyaloclastite, TT to 600 °C for 12 hours, and acquired using QEMSCAN at 20 µm resolution.

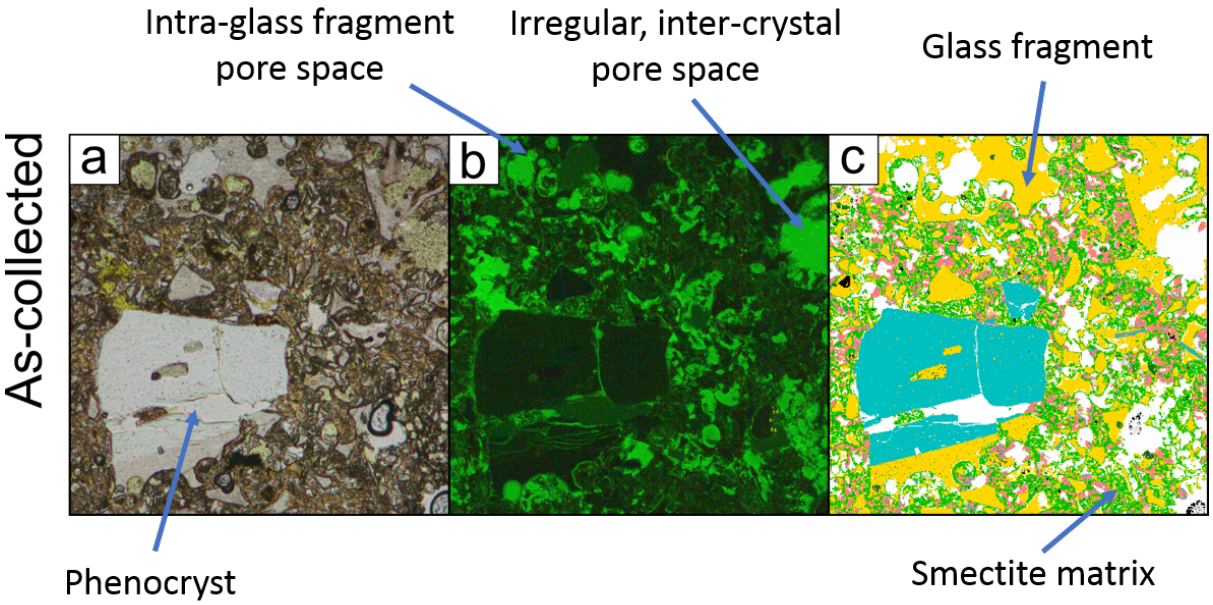

Figure S7. Annotated example from Figure 3 (main paper). a. Plain polarised light image from an optical microscope; b. Ultraviolet pore space map using florescent dyed thin section; c. QEMSCAN image showing mineral distribution

4. Additional Strength Curves

Figure 6c in the main paper presents a subset of the total tensile strength dataset, for easier viewing. Here, we present the other strength curves not shown in the main paper (Fig. S8).

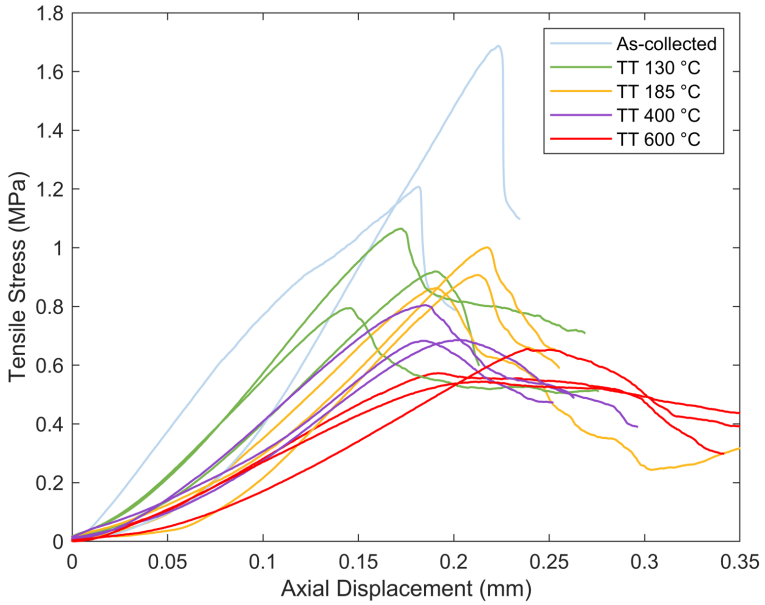

Figure S8. Additional tensile strength curves for as-collected and TT surficial material.